Earth Planet. Sci. Lett. 698 (2027) 120452

Contents lists available at ScienceDirect

Earth and Planetary Science Letters

journal homepage: www.elsevier.com/locate/epsl

Miocene surface uplift and moisture-source evolution resolved by stable-isotope proxies in the southern Central Andean foreland basin (~32°S)

Chance B. Ronemus [a,b,*], Caden J. Howlett [c,b], Peter G. DeCelles [b], Barbara Carrapa [b], Lucas M. Fennell [d], Kaustubh Thirumalai [b], Veleda A.P. Müller [e,b], Lucas Lothari [f]

[a] Department of Earth, Energy, and Environment, University of Calgary, Calgary, AB, Canada
[b] Department of Geosciences, The University of Arizona, Tucson, AZ, USA
[c] Department of Environmental Sciences, University of Montana Western, Dillon, MT, USA
[d] INGEIS–CONICET, Universidad de Buenos Aires, Buenos Aires, Argentina
[e] Geophysical Institute, University of Alaska Fairbanks, Fairbanks, AK, USA
[f] IANIGLA–CONICET, Mendoza, Argentina

ARTICLE INFO

Editor: Dr Andrew Zuza

Keywords:
Stable isotopes
Paleoaltimetry
Andes
Miocene
Mountain building
Volcanic glass
Foreland basin

ABSTRACT

How surface uplift is coupled to crustal shortening and thickening remains a central question in orogenic systems research. Existing stable-isotope records in the southern Central Andes show increasing $\delta^{18}O$ and δD values during Miocene retroarc shortening, inconsistent with expected enhanced orographic distillation. However, the role of changing climate and moisture source is underexplored in this region, where Pacific- and Atlantic-derived precipitation regimes meet. We pair pedogenic carbonate $\delta^{18}O/\delta^{13}C$ and volcanic glass δD from the Manantiales foreland basin (~32°S) with constraints from regional sedimentology to assess topographic and climatic evolution. Carbonate $\delta^{18}O$ and $\delta^{13}C$ values are high between ~37 and 18.6 Ma ($\delta^{18}O$ means −8.5 and −7.9 ‰), across a 33–21 Ma depositional hiatus, recording low paleoelevation in an arid foredeep. These values then decrease by ~4.5 ‰ between 18.6 and 18.3 Ma, interpreted to reflect surface uplift as the basin entered the wedge-top depozone. Glass δD values are consistently low after 17.9 Ma (−95.3 to −104.9 ‰), whereas carbonate $\delta^{18}O$ values increase by ~1.7 ‰ after ~16.5 Ma. We interpret this to record increased monsoonal moisture delivery during the Miocene Climatic Optimum and/or enhanced dry-season evaporation. Using isotope–elevation models accounting for ancient temperature and moisture-source changes, we calculate 1,886 m (68% CI: 1,446–2,255 m) of syndepositional surface uplift from carbonate $\delta^{18}O$, directionally consistent with glass δD. Surface uplift coincided with rapid crustal shortening and thickening, indicating coupled orogenic growth. These findings support model predictions that Andean mountain building alters isotopic signals by enhancing orographic distillation and shifting moisture-source regime.

1. Introduction

A central question in orogenic systems research is whether surface uplift tracks crustal shortening (e.g., Isacks, 1988) or is decoupled and modulated by other mechanisms (e.g., Garzione et al., 2017). Stable-isotope paleoaltimetry is widely used to address this question, but active mountain building can itself alter the climate system, convolving tectonic and climatic signals in the isotopic record (Ehlers and Poulsen, 2009; Insel et al., 2010). The Andes are Earth's archetypical active Cordilleran orogenic system and central to this debate. In the Central Andes, proxy records from southern sectors show gradual uplift tracking shortening, whereas those from northern regions have been interpreted to record punctuated uplift driven by episodic foundering of dense lower lithosphere (Canavan et al., 2014; Garzione et al., 2017; Quade et al., 2015; Sundell et al., 2019; Boschman, 2021, and references therein). In the southern Central Andes (~28–36°S), stable-isotope records remain comparatively sparse and have yielded trends conflicting with the enhanced orographic distillation expected under well-documented Miocene crustal shortening and thickening (Fennell et al., 2023; Giambiagi et al., 2022; Hoke et al., 2014; Muñoz-Gómez et al., 2025; Ruskin and Jordan, 2007).

Because progressive Rayleigh distillation of ascending air masses lowers precipitation $\delta^{18}O$ and δD values with increasing elevation (Poage and Chamberlain, 2001; Rowley, 2007), surface uplift is

* Corresponding author.
E-mail address: chance.ronemus@ucalgary.ca (C.B. Ronemus).

https://doi.org/10.1016/j.epsl.2026.120452
Received 14 May 2026; Received in revised form 24 October 2026; Accepted 26 October 2026
Available online 10 November 2026
0012-821X/© 2026 The Author(s). Published by Elsevier B.V. This is an open access article under the CC BY-NC license (http://creativecommons.org/licenses/by-nc/4.0/).

generally expected to drive decreases in the $\delta^{18}O$ values recorded by pedogenic carbonates ($\delta^{18}O_{carb}$) and the δD values recorded by volcanic glass (δD_{vg}) hydrated by environmental waters. Yet, reported $\delta^{18}O_{carb}$ values from the Manantiales and Cacheuta basins (Hoke et al., 2014) and δD_{vg} values from the Malargüe basin (Fennell et al., 2023) remain stable or increase during the Miocene, contradicting the decrease expected if shortening and thickening built high topography over this interval. This contradiction has two possible explanations: either surface uplift was genuinely decoupled from crustal thickening, or the isotopic signature of surface uplift has gone unrecognized, potentially masked by coeval changes in hydroclimate. The latter is plausible at these latitudes, which straddle the transition between Pacific-derived winter precipitation delivered by the westerlies and Atlantic-derived summer precipitation delivered by the South American Summer Monsoon (SASM; Figs. 1 & 2; Bookhagen and Strecker, 2008; Vuille et al., 2012). Shifts in the seasonal balance of these isotopically distinct moisture sources can alter precipitation $\delta^{18}O$ and δD values, masking or mimicking the isotopic signature of surface uplift (Hoke et al., 2013; Rohrmann et al., 2014).

Pedogenic carbonates and hydrated volcanic glass provide complementary stable-isotope records that can aid in disentangling climatic and topographic signals. Pedogenic carbonates form during discrete drying windows following major infiltration events and are thus biased by the largest precipitation events (Breecker et al., 2009; Huth et al., 2019). By contrast, volcanic glass hydrates continuously over 10^3–10^4 years after eruption and thus records amount-weighted mean annual precipitation (Dettinger and Quade, 2015; Cassel and Breecker, 2017). Evaporation can increase both δD_{vg} and $\delta^{18}O_{carb}$ (Nandy and Fan, 2025; Quade et al., 2007a,b; White et al., 2024), though paired records indicate the resulting negative bias on elevation estimates is smaller for δD_{vg} than $\delta^{18}O_{carb}$ (Jimenez-Rodriguez et al., 2022).

To date, these proxies have not been paired within a single basin segment in the southern Central Andes. The Manantiales basin (west–central Argentina; ~32°S) is an ideal target because it lies in the modern zone of moisture-source transition, is flanked on both sides by high (> 4 km) Andean topography, and preserves Eocene–Miocene foreland basin deposits containing both abundant pedogenic carbonate and vitric tuffs within a high-resolution chronostratigraphy (Figs. 1–4; Jordan et al., 1996). Recent studies have identified pre-18 Ma deposits (Pinto et al., 2018; Suriano et al., 2023; Ronemus et al., 2024) that were not sampled in the previous isotopic study of the basin by Hoke et al. (2014), which analyzed 78 pedogenic carbonates from the post-18 Ma section. The basin has been interpreted to record an early–middle Miocene transition from a foredeep to a wedge-top setting (Jordan et al., 1996; Ronemus et al., 2024), broadly coeval with rapid crustal shortening, thickening, and exhumation (Mackaman-Lofland et al., 2020; Carrapa et al., 2022; Howlett et al., 2025). However, whether surface uplift accompanied this deformation has yet to be resolved from the stable-isotope record.

This study adds 32 carbonate and 7 volcanic glass samples, extending the Manantiales basin's isotopic record to ca. 37 Ma. We document a previously unrecognized early Miocene decrease in $\delta^{18}O_{carb}$ to relatively low values consistent with δD_{vg}, followed by an increase in $\delta^{18}O_{carb}$ values during the middle Miocene that is absent in the δD_{vg} record. From these data, we calculate paleoelevations and estimate surface elevation change using representative isotope-elevation models simulating ancient climate conditions. Our results indicate that surface uplift was synchronous with crustal shortening and thickening, consistent with coupled orogenic growth. These findings underscore that extracting tectonic signals from isotope records requires explicit evaluation of orography, moisture source, and other climatic effects, particularly where topographic growth itself alters precipitation regime.

2. Background

2.1. Tectonic context of the southern Central Andes

The Andes are a Cordilleran orogenic system extending >7,000 km along the western margin of South America, developed above the subducting Nazca plate (Fig. 1a; e.g., Isacks, 1988; Ramos, 2009). At ~32°S, the orogen consists of (west to east): the Coastal Cordillera forearc margin; deformed Mesozoic–Cenozoic sedimentary and volcanic rocks of the Principal Cordillera, including the western fold-thrust belt and now-inactive Cenozoic magmatic arc; Permo–Triassic igneous rocks exposed along reverse faults in the Frontal Cordillera; the Precordillera thin-skinned fold-thrust belt; and the Sierras Pampeanas basement-cored uplifts, which segment the modern foreland (Fig. 1b; Ramos, 2009; Farías et al., 2008; Mackaman-Lofland et al., 2020; Giambiagi et al., 2022).

At this latitude, Cenozoic foreland basin subsidence initiated at ca. 39–33 Ma, attributed to retroarc shortening within the western Principal and Frontal Cordilleras on the basis of provenance data (Suriano et al., 2023; Ronemus et al., 2024). During the Oligocene, subsidence ceased while the Abanico basin developed in the western Principal Cordillera, preserving normal fault-related growth geometries and geochemical signatures indicating intra-arc extension (Jara and Charrier, 2014; Charrier et al., 2024). Foreland basin deposition resumed after ca. 21 Ma (Buelow et al., 2018; Pinto et al., 2018), and tectonic inversion of the Abanico basin and exhumation in the Frontal Cordillera is resolved by ca. 18 Ma (Howlett et al., 2025; Mpodozis et al., 2009; Perelló et al., 2012). By ca. 14–12 Ma, the thrust front propagated eastward into the Precordillera, followed by slab flattening, magmatic shutoff, and intra-foreland uplift of the Sierras Pampeanas (Howlett et al., 2025; Mackaman-Lofland et al., 2020; Ramos, 2009). Whole-rock and zircon igneous geochemical data indicate that ~20 km of hinterland crustal thickening occurred during early–middle Miocene shortening (Carrapa et al., 2022; Muñoz-Gómez et al., 2025). Assuming Airy isostasy, this predicts significant surface uplift that is so far unrecognized in the stable-isotope record.

2.2. Depositional context of the Manantiales Basin

The Manantiales basin is a north–south–elongate depocenter bound by uplifted blocks of the Frontal Cordillera (Figs. 1b & 3; Jordan et al., 1996). The basin fill, consisting of the upper Eocene Río de los Patos and lower–middle Miocene Chinches formations, rests unconformably on Permian basement of the Cordillera del Tigre to the east and is cut by the Espinacito fault to the west (Fig. 3; Suriano et al., 2023; Ronemus et al., 2024). The Río de los Patos Formation (ca. 39–33 Ma) consists of playa, alluvial plain, and eolian deposits that accumulated in a distal foredeep setting, followed by a ca. 12 Myr hiatus attributed to forebulge passage (Ronemus et al., 2024) or cessation of flexural subsidence during Abanico basin extension (Fig. 4a, e; Suriano et al., 2023; Ronemus, 2025). The overlying Chinches Formation (ca. 21.1–11 Ma) is >4 km thick and records a broadly upward-coarsening succession with age constraints from zircon U–Pb, hornblende $^{40}Ar/^{39}Ar$, and magnetostratigraphy (Fig. 4a, e; Jordan et al., 1996; Ronemus et al., 2024, and references therein). The formation records a transition from transverse fluvial (member 1; ca. 21–18 Ma), to axial fluvial (member 2; ca. 18–16 Ma), to internally drained lacustrine (member 3; ca. 16–15.5 Ma), to prograding alluvial fan deposits (member 4, ca. 15.5–11 Ma; Fig. 4a, e; member designations of Ronemus et al. 2024).

Whereas Jordan et al. (1996) favored a model in which the basin accumulated mainly in a foredeep depozone, Ronemus et al. (2024)

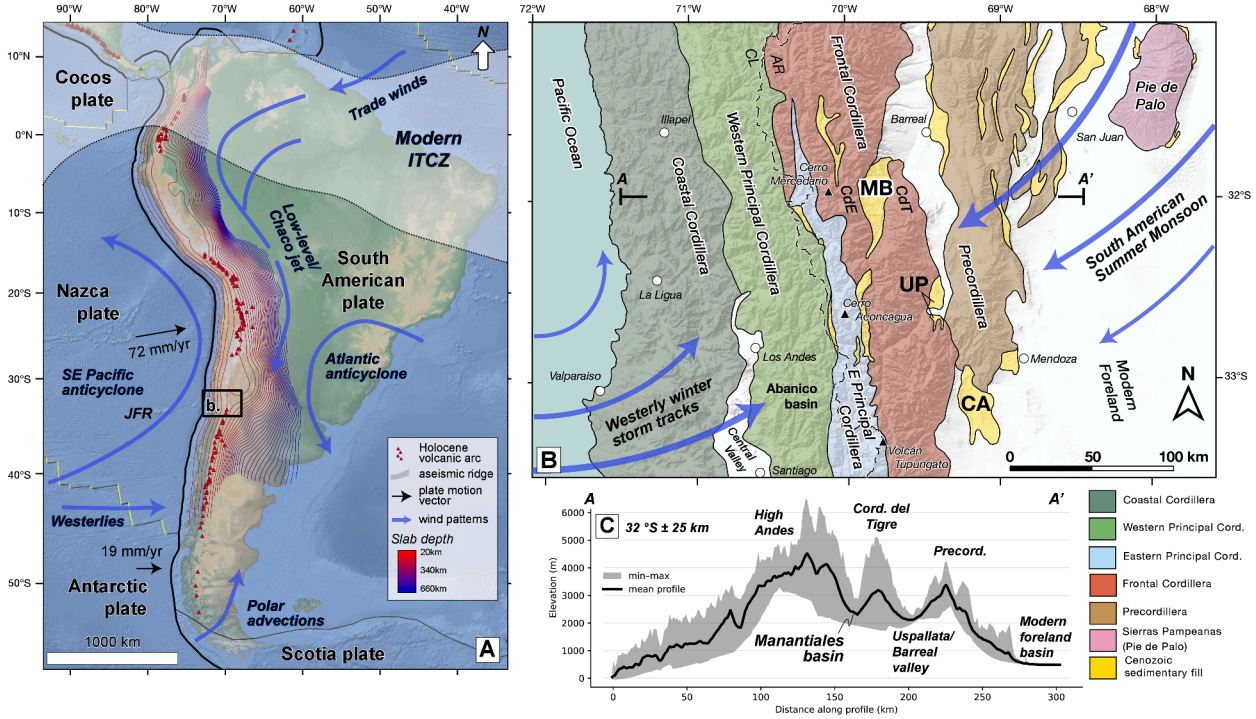

Fig. 1. (a) Plate tectonic and climatic context of South America, showing slab-depth contours (Slab 2.0 model), plate-motion vectors, and principal circulation features (Garreaud et al., 2009). These synoptic patterns frame the seasonal end-members used in this study. Modified from Ronemus et al. (2024) and data sources cited therein. Black, gray, and yellow lines mark subduction zones, transform faults, and spreading ridges, respectively; JFR—Juan Fernández Ridge. (b) Tectonomorphic map of the southern Central Andes from the Coastal Cordillera to the modern broken foreland, highlighting the Manantiales basin (MB) and select nearby exposures of foreland basin fill (UP—Uspallata basin; CA—Cacheuta basin). Dominant seasonal wind patterns are schematically indicated. Modified from Ronemus et al. (2024). Other abbreviations: AR—Argentina; CL—Chile; CdE—Cordón del Espinacito; CdT—Cordillera del Tigre. (c) Topographic swath profile at 32°S (± 25 km) constructed from SRTM data, situating the MB relative to the High Andes, Cordillera del Tigre, and the modern foreland.

argued that unconformity development followed by drainage internalization and changes in detrital zircon provenance together indicate transfer of the basin into the wedge-top depozone (*sensu* DeCelles and Giles, 1996) during uplift of the eastward-adjacent Cordillera del Tigre between ca. 19 and 15 Ma. Unequivocal deformation on the western basin margin is recorded after ca. 15 Ma by growth geometries in member 4 related to slip on the Espinacito fault (Ronemus et al., 2024). Deposition continued until ca. 11 Ma, after which thermochronology indicates basin inversion during propagation of the orogenic wedge into the Precordillera (Mackaman-Lofland et al., 2020; Howlett et al., 2025).

2.3. Regional climate and its evolution

Modern precipitation in the southern Central Andes derives from (1) winter Southern Hemisphere westerlies on the western flank and (2) SASM moisture advected along the eastern flank by the South American low-level jet (SALLJ; Fig. 1; Garreaud et al., 2009; Vuille et al., 2012). Winter precipitation dominates the western slope and crest and follows a steep isotopic lapse rate, producing very low $\delta^{18}O$ values at elevation; summer precipitation, falling mainly on the foreland and eastern flank, arrives with higher $\delta^{18}O$ values and has a weaker lapse rate with elevation (Hoke et al., 2013; Rohrmann et al., 2014). The composite isotope–elevation relationship of precipitation in this sector therefore deviates from simple Rayleigh expectations and varies with mixing ratio between these seasonal end-members (Hoke et al., 2013; Insel et al., 2013; Rohrmann et al., 2014). The Manantiales basin lies in a transition between these moisture sources, both in terms of latitude and elevation (Figs. 1a–b & 2; Bookhagen and Strecker, 2008). Modern spring waters from the basin yield $\delta^{18}O$ values ~2.5‰ higher than those collected at similar elevation (~3,200 m) west of the Cordón del Espinacito (Calvi et al., 2024), suggesting a present bias toward the SASM end-member.

The study interval (ca. 21–14 Ma) spans a major regional climate transition that further complicates stable isotope-based paleoaltimetry. During the Oligocene–early Miocene, sedimentary evidence suggests that arid environments such as eolian dune fields and evaporative playas were widespread across the southern Central Andean foreland basin, interpreted to indicate limited moisture penetration (Starck et al., 2024; George et al., 2025). Regional replacement of these facies by fluvial and lacustrine deposits between ca. 18 and 15 Ma has been interpreted to record a shift toward more humid conditions due to intensification of the SASM during the Miocene Climatic Optimum (MCO; George et al., 2025), a warming event associated with elevated pCO_2 (Super et al., 2018) and global temperatures several degrees above modern (Goldner et al., 2014).

Climate models suggest that growth of Andean topography itself modulated foreland moisture delivery by blocking the Pacific westerlies and initiating the SALLJ, which channels tropical moisture feeding the SASM southward along the eastern Andean flank (Ehlers and Poulsen, 2009; Insel et al., 2010). At plateau latitudes (~15–25°S), the resulting increase in precipitation amount lowers $\delta^{18}O$ values, producing isotopic shifts that mimic surface uplift (Ehlers and Poulsen, 2009). At ~32°S, however, evidence for early Miocene foreland aridity suggests limited summer moisture penetration; this implies that the pre-existing moisture budget was dominated by Pacific-derived winter precipitation with characteristically low $\delta^{18}O$ values (Hoke et al., 2013; Insel et al., 2013). Therefore, the introduction of higher-$\delta^{18}O$ Atlantic-derived summer moisture by an invigorated SASM, as suggested by ca. 18–15 Ma foreland humidification, might raise $\delta^{18}O$ values and mask the isotopic

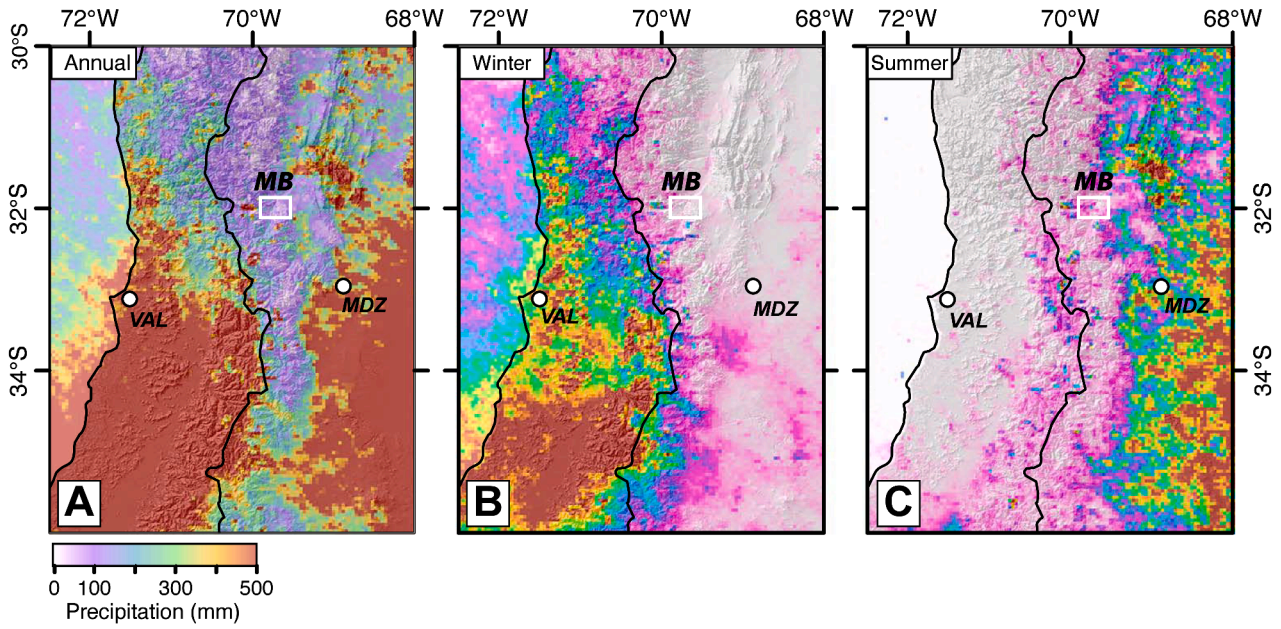

Fig. 2. Modern precipitation climatology near the Manantiales Basin (MB). Panels show (a) annual, (b) austral winter (cool season), and (c) austral summer (warm season) precipitation, derived from Tropical Rainfall Measuring Mission data spanning 1998 to 2009 (Bookhagen and Strecker, 2008). Black line marks the international border, white box denotes the Manantiales basin, and white circles mark meteorologic stations in Valparaíso (VAL) and Mendoza (MDZ), whose data anchor the Rayleigh distillation models used herein. The western flank of the Andes is dominated by winter precipitation, although spillover occurs mainly south of ~33°S; summer precipitation falls mainly on the eastern flank of the Andes. The modern Manantiales basin lies at the transition between these seasonal end-members. Modified from Hoke et al. (2013).

expression of concurrent uplift. Extracting tectonic signals from the isotopic record in this region thus requires explicit treatment of moisture-source variability through time.

3. Materials and methods

3.1. Volcanic glass hydrogen isotopes

We measured hydrogen isotope ratios ($^2H/^1H$) in volcanic glass from 7 vitric airfall tuffs interbedded with fluvial and alluvial fan facies of the Chinches Formation (Figs. 3 & 4). Glass was isolated using magnetic and density separation, then cleaned following protocols described by Cassel and Breecker (2017, details in Text S1). Measurements used high-temperature conversion (TC/EA; 1,400 °C) coupled to a Thermo Electron Delta V mass spectrometer at the University of Arizona Environmental Isotope Laboratory. Glass H_2O wt% was recorded as a hydration check, and samples with H_2O >9 wt.% were flagged and excluded from paleoelevation calculations due to potentially incomplete removal of adhering clay or zeolite phases (Cassel and Breecker, 2017). Results are reported as δD_{vg} in per mille (‰) relative to Vienna Standard Mean Ocean Water (VSMOW), with 1σ precision of ±2.0‰ based on internal standards. We report mean and 1σ of 2–4 replicates per sample.

3.2. Carbonate oxygen and carbon isotopes

We analyzed stable oxygen ($^{18}O/^{16}O$) and carbon ($^{13}C/^{12}C$) isotope ratios of 32 carbonate samples from the Manantiales basin (Figs. 3 & 4), complementing the dataset of Hoke et al. (2014). We collected pedogenic micritic carbonate nodules (n = 20), rhizocretions (n = 2), phreatic calcrete lenses (n = 6), and sparry calcite (n = 4) from fluvial and alluvial fan deposits of the Eocene Río de los Patos Formation (n = 5) and the Miocene Chinches Formation (n = 27; morphology descriptions in Text S2). Samples were analyzed using a Kiel IV Carbonate Device coupled to a MAT 253+ isotope ratio mass spectrometer at the University of Arizona Paleo^2 Laboratory; 28 samples were analyzed in duplicate and 4 as single aliquots, reported as means ±1σ or pooled 1σ, respectively. Oxygen and carbon stable-isotope results are reported as $\delta^{18}O_{carb}$ and $\delta^{13}C_{carb}$, respectively, in per mille (‰) relative to Vienna Pee Dee Belemnite (VPDB). Replicate analyses of IAEA-603 ($n = 11$) yielded 1σ reproducibility of 0.04 ‰ ($\delta^{13}C$) and 0.07 ‰ ($\delta^{18}O$), consistent with long-term precision for this setup.

3.3. Calculation of paleo-environmental water isotopes

To enable more direct comparison between proxies, we calculated environmental water $\delta^{18}O_{env}$ (VSMOW) from $\delta^{18}O_{carb}$ and δD_{vg}. For carbonates, we converted $\delta^{18}O_{carb}$ (VPDB) to VSMOW and applied calcite–water fractionation following Kim and O'Neil (1997):

$$\delta^{18}O_{carb,VSMOW} = 1.03091\,\delta^{18}O_{carb,VPDB} + 30.91,$$
$$\delta^{18}O_{env,carb} = \frac{\delta^{18}O_{carb,VSMOW} + 1000}{\alpha_{cal\text{-}H_2O}} - 1000, \quad (1)$$

where $1000 \ln \alpha_{cal\text{-}H_2O} = 18.03(1000/T) - 32.42$ and T is in Kelvin. We used a constant $T = 20 \pm 2.5$°C (1σ) based on regional clumped-isotope temperatures measured in modern soil carbonates (Peters et al., 2013). Sensitivity to formation-temperature uncertainty, including possible MCO soil warming, is evaluated in Text S4. Spar samples were excluded due to uncertain formation temperature.

For glass, we converted δD_{vg} to $\delta D_{env,vg}$ using the Friedman et al. (1993) fractionation factor ($\alpha_{vg\text{-}H_2O} = 0.9668 \pm 0.0005$), then estimated $\delta^{18}O_{env,vg}$ via the local meteoric water line (LMWL) from Hoke et al. (2013):

$$\delta D_{env} = \frac{\delta D_{vg} + 1000}{\alpha_{vg\text{-}H_2O}} - 1000, \quad \delta^{18}O_{env,vg} = \frac{\delta D_{env} - 11.75}{8.29}. \quad (2)$$

Samples hydrated by evaporatively enriched waters may deviate from the LMWL, as discussed in Section 5.2. Varying the LMWL slope from 8.29 to 8.0 (global MWL) decreases individual $\delta^{18}O_{env,vg}$ estimates by ≤0.5 ‰.

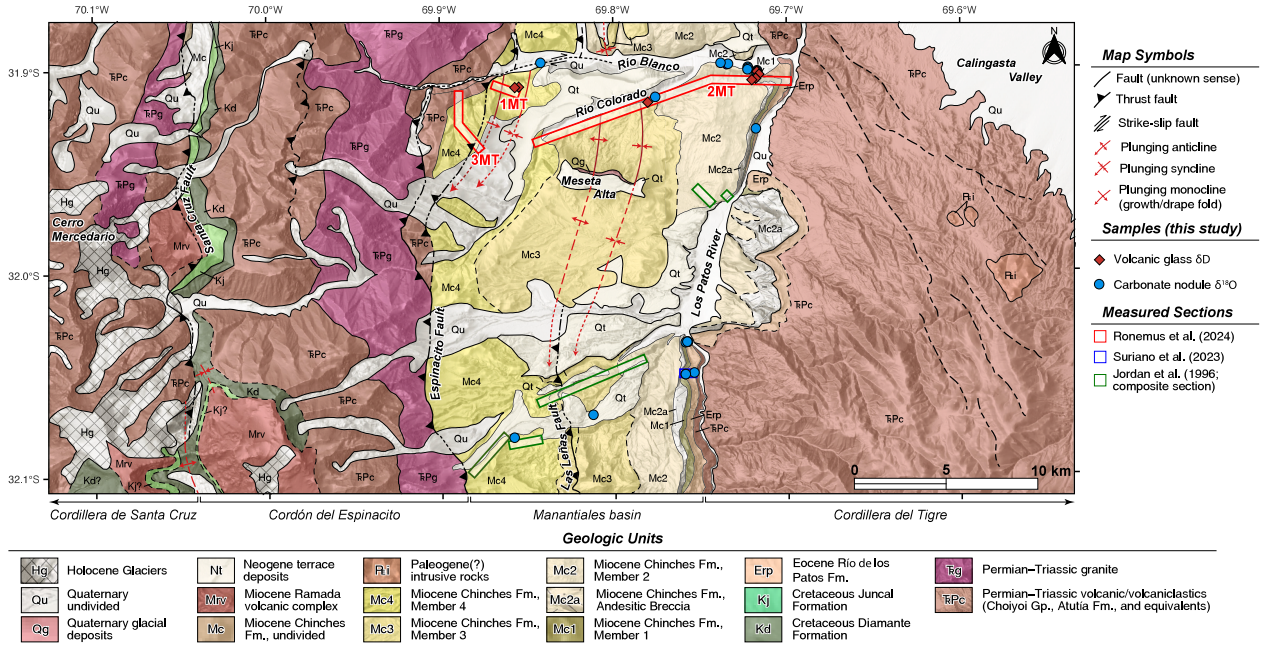

Fig. 3. Geologic map of the Manantiales basin, adapted and updated from Ronemus et al. (2024). Assignment of the Juncal and Diamante formations in the western map area is based on mapping and geochronology results of Ronemus (2025, Appendix D). Queried units denote uncertain assignments. Faults and contacts are dashed where inferred, and faults are dotted where concealed. Sample locations for volcanic glass (δD) and pedogenic carbonate (δ^{18}O, δ^{13}C) are shown, linking our isotopic datasets to measured sections of Jordan et al. (1996), Suriano et al. (2023), and Ronemus et al. (2024).

3.4. Paleoelevation estimates

Because modern precipitation at ~32°S mixes isotopically distinct seasonal moisture sources (Fig. 2; Hoke et al., 2013; Insel et al., 2013), we calculated paleoelevation using three representative isotope–elevation models. We recomputed each varying initial source-region temperature and source-water δ^{18}O to simulate Eocene–Miocene conditions, propagating associated uncertainties into elevation estimates (Text S3). The first two are seasonal end-member Rayleigh distillation curves computed with a one-dimensional pseudo-adiabatic parcel model (see Text S3; Rowley et al., 2001; Rowley, 2007). The winter curve is anchored to meteorological station data from Valparaíso, Chile, representing westerly-derived moisture; the summer curve is anchored to data from Mendoza, Argentina, representing moisture delivered by the SASM (Fig. 2; based on the source parameters of Hoke et al., 2013). The third is a mixed-season empirical model based on the relationship derived from modern precipitation at ~33°S by Hoke et al. (2013):

$$z = -7.2\,(\delta^{18}\mathrm{O})^2 - 314.8\,(\delta^{18}\mathrm{O}) - 367.6, \quad (3)$$

where elevation is in meters and coefficient standard errors (1σ) are 4.7, 115.1, and 621.7, respectively (Hoke et al., 2013). Because this relationship integrates both seasonal sources at their present proportions, it assumes moisture mixture similar to modern. We represent it as an elevation-dependent mixture of the winter and summer end-member curves fit to the polynomial, so that it inherits their response to changes in initial source-region temperature and source-water δ^{18}O. Model details, boundary-condition parameters, and selection rationale are provided in Text S3.

We simulated ancient climate conditions by imposing the following shifts, with uncertainties resampled within the Monte Carlo simulation. We imposed initial source-region temperatures warmer than modern by $+5 \pm 3$ °C for Eocene–Oligocene samples, $+4 \pm 2$ °C for pre-MCO Miocene samples, and $+5 \pm 2.5$ °C for MCO-interval samples, based on regional sea-surface temperature estimates (Text S3). We increased the initial δ^{18}O composition of each curve by 0.29 ± 0.10 ‰ for every °C of simulated warming, following the temporal isotope–temperature slope applied by Fennell et al. (2023, see Text S3). Finally, we imposed a uniform source-water δ^{18}O offset of -0.6 ± 1.0 ‰ reflecting ^{16}O-enriched seawater during the Miocene (Miller et al., 2020).

For each model, paleoelevations were calculated for sample subsets defined by proxy type and stratigraphic interval (carbonate Groups A–E and glass Groups II–III; Table 1). The preferred model for each group is identified by inferred moisture regime (see Section 5 and Text S3.6). Uncertainties were calculated using a Monte Carlo simulation (100,000 iterations), which propagates per-sample analytical error, inter-sample scatter, calibration uncertainties, and uncertainties on the boundary-condition values described above. We report median values with 68% confidence intervals (~1σ). Our full analysis workflow is provided in Script S1, and sensitivity tests and uncertainty propagation details are given in Text S4.

4. Results

4.1. Volcanic glass hydrogen isotopes

Results of our volcanic glass analyses are reported in Table 1 (analytical data in Dataset S1) and shown graphically in Fig. 4d. Four of seven volcanic glass samples yielded H_2O contents of 2.8–6.3 wt%, within the typical range of glass hydrated to saturation (Cassel and Breecker, 2017; Nandy and Fan, 2025). Sample 1MT416 yielded a low value of 1.0 wt%. Because the exceptionally negative δD_{vg} of this sample (−110.3 ‰) argues against significant contamination by ^{2}H-enriched magmatic water (typically ≥ −80 ‰; Seligman et al., 2016), we retain it for further interpretation. Samples 2MT528A and 2MT528B from a ca. 18.6 Ma tuff yielded elevated H_2O contents of 10.8 and 10.1 wt%, potentially indicative of clay or zeolite alteration, and are thus excluded from paleoelevation calculations and interpretation.

δD_{vg} of our samples ranges from −110.3 ‰ to −74.1 ‰, with an overall mean of −95.8 ± 13.3 ‰ (1σ; Table 1; Fig. 4d). Four samples collected from the lower Chinches Formation comprise two age clusters. The first cluster (ca. 18.6 Ma; $n = 2$; hereafter Glass Group I) yielded a mean δD of −82.4 ± 11.7 ‰ but was excluded for elevated

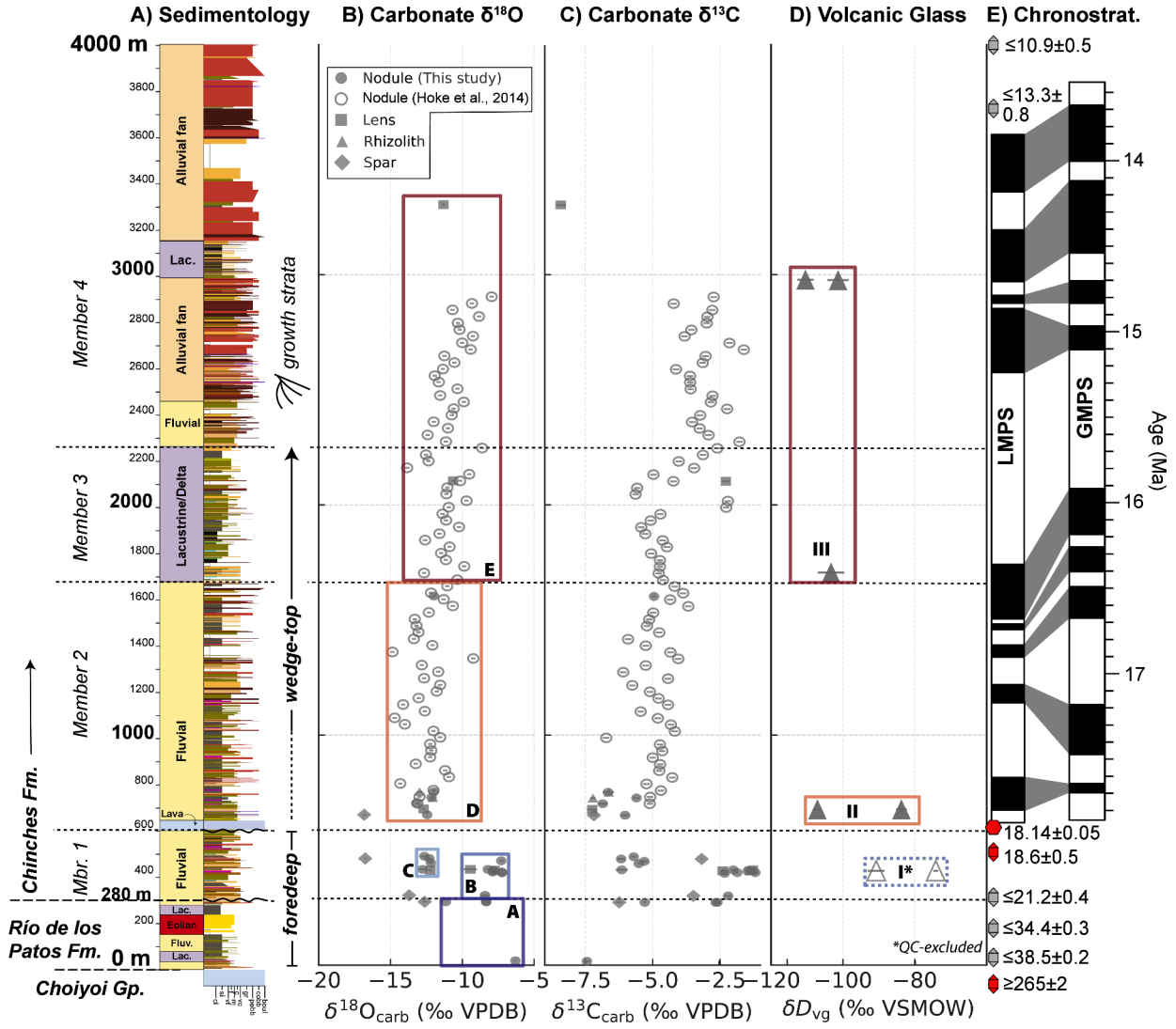

Fig. 4. Stratigraphic distribution of facies and isotopes in the Manantiales basin fill. (a) Simplified measured stratigraphic column, showing bed thickness, grain size, and lithofacies (from Ronemus et al. 2024; see their lithofacies legend), along with interpreted depositional environment (left column; Lac.—lacustrine). (b) $\delta^{18}O_{carb}$ (VPDB) and (c) $\delta^{13}C_{carb}$ (VPDB) of carbonate samples (open circles from Hoke et al. 2014) and (d) δD_{vg} (VSMOW) of volcanic glass are shown by stratigraphic position. Colored boxes in (b) and (d) denote sample groups discussed in the text. Glass Group I is excluded from interpretation due to high H_2O contents (>9 wt.%). Horizontal error bars reflect 1σ analytical uncertainty and are smaller than the symbol where not visible. Age uncertainty is evident by comparing sample position to (e), showing a summary of chronostratigraphic controls on the Manantiales basin fill. Left column shows local magnetic polarity stratigraphy (MPS) of Jordan et al. (1996), which was recorrelated to the global MPS by Ronemus et al. (2024) based on tuff (red bipyramid) and detrital (gray bipyramid) zircon U-Pb and hornblende $^{40}Ar/^{39}Ar$ (red hexagon) geochronologic constraints (Pinto et al., 2018; Mackaman-Lofland et al., 2020; Suriano et al., 2023; Ronemus et al., 2024; Rocher et al., 2024, and references therein).

H_2O. The second cluster consists of two ca. 17.9 Ma samples (Glass Group II) with a mean δD of −95.3 ± 16.5 ‰. Three samples collected from higher in the section (ca. 15.8–14.1 Ma; Glass Group III) yielded more negative values of −104.9 ± 4.8 ‰, which are similar across time (Fig. 4d).

4.2. Carbonate oxygen and carbon isotopes

Carbonate $\delta^{18}O_{carb}$ and $\delta^{13}C_{carb}$ results are shown in Table 1 and Fig. 4b–c (analytical data in Dataset S2). Carbonate samples yielded $\delta^{18}O_{carb}$ and $\delta^{13}C_{carb}$ in the range of −16.8 ‰ to −6.3 ‰ and −9.3 ‰ to −1.0 ‰, respectively. Samples of sparry calcite yielded the most negative $\delta^{18}O_{carb}$ (−15 ± 2.1 ‰; 1σ) and variable $\delta^{13}C_{carb}$ (−5.4 ± 2.3 ‰). Micritic samples collectively have $\delta^{18}O_{carb}$ and $\delta^{13}C_{carb}$ means of −10.3 ± 2.3 ‰ and −4.7 ± 2.7 ‰, respectively. Values for micritic samples are not strongly correlated with sample type (i.e., nodules, lenses, rhizocretions).

Mean $\delta^{18}O_{carb}$ of samples from the Río de los Patos Formation (hereafter Group A) is −8.5 ± 2.0 ‰, whereas $\delta^{13}C_{carb}$ shows scatter from −8.2 ‰ to −2.6 ‰. Samples from the lower Chinches Formation define two compositional end-members, hereafter referred to as Groups B and C. Group B comprises relatively high $\delta^{18}O_{carb}$ and $\delta^{13}C_{carb}$ values (−7.9 ± 0.7 ‰ and −2.0 ± 1.5 ‰, respectively; n = 9) spanning ca. 18.8–18.3 Ma. Group C comprises relatively low $\delta^{18}O_{carb}$ and $\delta^{13}C_{carb}$ values (−12.5 ± 0.2 ‰ and −6.1 ± 1.8 ‰, respectively; n = 7) and spans ca. 18.6–17.9 Ma. Group B isotopic signatures are exclusive before ca. 18.6 Ma and absent after ca. 18.3 Ma. Group D samples from overlying ca. 17.8–16.5 Ma deposits (n = 5 + 29 of Hoke et al., 2014) yielded mean $\delta^{18}O_{carb}$ and $\delta^{13}C_{carb}$ of −12.6 ± 1.1 ‰ and −5.6 ± 1.0 ‰, respectively, overlapping with Group C. Group E samples from

Table 1
Summary of new stable-isotope data from the Manantiales Basin. 'Groups' refer to sample subsets defined in the text. †Glass Group I is QC-excluded (H_2O > 9 wt.%; see text).

Sample Name	Strat. level (m)	Age (Ma)	Group	Proxy	Type	$\delta^{18}O_{carb}$ (‰, VPDB)	±1σ	$\delta^{13}C_{carb}$ (‰, VPDB)	±1σ	δD_{vg} (‰, VSMOW)	±1σ	$\delta^{18}O_{env}$ (‰, VSMOW)	±1σ
MT24C2	3300	14.1	E	Carbonate	Lens	–11.31	0.08	–9.32	0.22	—	—	–9.97	0.52
1MT416	2975	14.1	III	Glass	Tuff	—	—	—	—	–110.33	2.31	–11.04	0.29
1MT418	2973	14.1	III	Glass	Tuff	—	—	—	—	–101.27	2.96	–9.91	0.37
MT24C1	2100	15.5	E	Carbonate	Lens	–10.64	0.15	–2.21	0.14	—	—	–9.3	0.54
MT-TF-01	1703	15.8	III	Glass	Tuff	—	—	—	—	–103.22	3.67	–10.15	0.46
MT24C13	1600	16.0	E	Carbonate	Nodules	–11.98	0.05	–5.31	0.11	—	—	–10.64	0.52
MT24C22n	750	17.6	D	Carbonate	Nodules	–11.98	0.06	–7.29	0.22	—	—	–10.64	0.52
MT24C22r	750	17.6	D	Carbonate	Rhizolith	–12.97	0.2	–7.25	0.23	—	—	–11.63	0.55
MT24C23.1	725	17.7	D	Carbonate	Nodules	–12.14	0.15	–6.06	0.14	—	—	–10.8	0.54
MT24C23.2	725	17.7	D	Carbonate	Rhizolith	–12.05	0.04	–7.93	0.11	—	—	–10.71	0.52
MT24C20	700	17.8	D	Carbonate	Nodules	–13.21	0.04	–7.51	0.21	—	—	–11.87	0.52
MT24C19	675	17.9	C	Carbonate	Lens	–12.69	0.11	–7.97	0.22	—	—	–11.35	0.53
MT23TF02	675	17.9	II	Glass	Tuff	—	—	—	—	–107.0	1.00	–10.62	0.14
MT23TF03	675	17.9	II	Glass	Tuff	—	—	—	—	–83.67	1.53	–7.71	0.20
MT24C18	650	18.0	C	Carbonate	Nodules	–12.45	0.01	–6.55	0.18	—	—	–11.11	0.52
MT24C21s	650	18.0	—	Carbonate	Spar	–16.83	0.13	–7.89	0.16	—	—	—	—
MT24C17	470	18.2	C	Carbonate	Nodules	–12.65	0.23	–6.18	0.11	—	—	–11.31	0.57
MT24C11	460	18.2	—	Carbonate	Spar	–16.76	0.08	–3.26	0.04	—	—	—	—
MT24C16	460	18.2	C	Carbonate	Nodules	–12.3	0.13	–6.72	0.17	—	—	–10.96	0.54
MT24C12	450	18.3	B	Carbonate	Nodules	–7.29	0.16	–5.72	0.16	—	—	–5.94	0.54
MT24C15	440	18.4	C	Carbonate	Nodules	–12.18	0.13	–5.96	0.04	—	—	–10.84	0.53
MT24C7	413	18.5	B	Carbonate	Lens	–9.45	0.47	–1.05	0.04	—	—	–8.11	0.70
MT24C10	413	18.5	B	Carbonate	Nodules	–8.23	0.07	–1.9	0.11	—	—	–6.88	0.52
MT24C14	413	18.5	C	Carbonate	Nodules	–12.77	0.24	–6.7	0.26	—	—	–11.43	0.57
MT24C8	409	18.6	C	Carbonate	Lens	–12.22	0.10	–2.35	0.07	—	—	–10.88	0.53
MT24C6	409	18.6	B	Carbonate	Lens	–7.76	0.01	–1.17	0.08	—	—	–6.41	0.52
MT24C5m	408	18.6	B	Carbonate	Nodules	–7.81	0.06	–1.28	0.08	—	—	–6.47	0.53
2MT528A†	408	18.6	I†	Glass	Tuff	—	—	—	—	–74.12	0.7	–6.52	0.11
2MT528B†	408	18.6	I†	Glass	Tuff	—	—	—	—	–90.67	2.31	–8.59	0.29
MT24C3a	401	18.7	B	Carbonate	Nodules	–7.89	0.03	–1.73	0.04	—	—	–6.55	0.52
MT24C3b	401	18.7	B	Carbonate	Nodules	–7.25	0.01	–0.95	0.07	—	—	–5.9	0.52
MT24C4	398	18.7	B	Carbonate	Nodules	–7.23	0.02	–2.26	0.08	—	—	–5.89	0.52
MT24C9	300	18.8	B	Carbonate	Nodules	–8.43	0.32	–2.12	0.14	—	—	–7.08	0.61
MT24C5s	300	18.8	—	Carbonate	Spar	–13.7	0.01	–3.61	0.01	—	—	—	—
4MT50	272	33.0	A	Carbonate	Nodules	–11.15	0.01	–5.7	0.06	—	—	–9.81	0.52
RPC2a	272	33.0	A	Carbonate	Nodules	–8.35	0.14	–2.65	0.03	—	—	–7.01	0.54
RPC2b	272	33.0	A	Carbonate	Nodules	–8.33	0.15	–2.58	0.14	—	—	–6.99	0.54
RPC3	272	33.0	—	Carbonate	Spar	–12.62	0.15	–6.8	0.14	—	—	—	—
RPC1	16	37.0	A	Carbonate	Nodules	–6.31	0.05	–8.19	0.14	—	—	–4.96	0.53

ca. 16.4–14.1 Ma deposits ($n = 3 + 49$ of Hoke et al., 2014) yield higher $\delta^{18}O_{carb}$ and $\delta^{13}C_{carb}$ of -10.9 ± 1.1 ‰ and -4.0 ± 1.4 ‰, respectively.

4.3. Water-equivalent isotopes ($\delta^{18}O_{env}$) and paleoelevation

Water-equivalent $\delta^{18}O_{env}$ (VSMOW; Table 1; Fig. 5) mirrors trends in the unconverted data. Glass and carbonate $\delta^{18}O_{env}$ values overlap prior to ca. 15.5 Ma but diverge thereafter, with increasing $\delta^{18}O_{env,carb}$ and approximately stable $\delta^{18}O_{env,vg}$ values (Fig. 5).

Paleoelevation estimates from the three isotope–elevation models are compiled in Table 2 and visualized in Figs. 6 and 7a. Glass paleoelevations from the winter Rayleigh model are 1.54 [68% CI: 0.84–2.36] km for Group II (ca. 17.9 Ma) and 2.17 [1.44–3.03] km for Group III (15.8–14.1 Ma). The mixed-season empirical model yields higher elevations of 2.27 [1.82–2.72] and 2.62 [2.21–3.01] km for Groups II and III, respectively. The summer Rayleigh model yields elevations of 4.24–5.12 km, far exceeding the modern basin elevation of 2.36–2.90 km.

Carbonate-derived paleoelevations using the winter model are 0.92 [0.20–1.87] km for Group A (Río de los Patos Fm.). Group B (Chinches Fm.) yields 0.52 [0.00–1.18] km (lower bound truncated at sea level), whereas Group C yields 2.22 [1.54–2.98] km. Group D yields 2.25 [1.57–3.02] km, and Group E yields 1.88 [1.16–2.74] km. The mixed-season empirical model yields 1.90 [1.39–2.51], 1.64 [1.25–2.07], 2.63 [2.26–2.99], 2.65 [2.28–3.01], and 2.48 [2.03–2.89] km for Groups A through E, respectively. Summer-curve estimates of 2.93–5.16 km likewise exceed the modern mean basin elevation. Preferred model selection and resulting surface uplift estimates are discussed below.

5. Discussion

Our stable-isotope dataset reveals three key features that bear on the relationship between climate, shortening, and surface uplift. (1) Carbonates yield relatively high $\delta^{18}O$ and $\delta^{13}C$ values prior to ca. 18.6 Ma. (2) These values shift markedly lower between 18.6 and 18.3 Ma, to a state consistent with Group II glass δD values. (3) Carbonate $\delta^{18}O$ values increase after ca. 16.5 Ma, whereas glass δD values do not. We first evaluate whether secondary alteration or evaporative enrichment can account for these patterns, and then consider evolving basin setting and moisture source. Finally, we synthesize surface uplift estimates and consider their tectonic implications (Figs. 7 & 8).

5.1. Consideration of secondary alteration

Resetting of $\delta^{18}O$ by secondary alteration following burial has been shown to influence many paleoaltimetry proxies and may be difficult to detect in carbonate samples (Quade et al., 2020). Experiments indicate that δD values of unaltered hydrated glass are stable even in the presence of diagenetic fluids (Cassel and Breecker, 2017), and secondary alteration typically produces clay or zeolite phases which are detectable optically and through elevated H_2O contents. On this basis, the two Group I samples that show elevated H_2O contents (>9 wt.%) are excluded. Other



Fig. 5. (a) Calculated $\delta^{18}O$ (VSMOW) of paleo-environmental water through time for Manantiales Basin micritic carbonate (circles) and volcanic glass (triangles). Previously published Cacheuta basin carbonates from Hoke et al. (2014), recorrelated to the chronostratigraphy of Buelow et al. (2018), are shown for regional context (gray diamonds). Samples are colored by groups described in the text and shown in Fig. 4. X-axis is broken at 20 Ma, showing Río de los Patos Formation samples left of the break and Chinches Formation samples to the right. All conversions follow fractionation parameters described in the Methods. Shaded region denotes the Miocene Climatic Optimum (MCO; ~17–14 Ma). (b) Median and interquartile range of $\delta^{18}O_{env}$ values from regional basins grouped by inferred depozone, from this study and Hoke et al. (2014). Parentheticals for Manantiales labels indicate carbonate groups. The Uspallata sections are not plotted in (a) because they lack precise age control.

Table 2
Paleoelevation medians with 68% confidence intervals (km) from three isotope–elevation models, modified for age-matched climate conditions (see text): Rayleigh winter (west-derived), mixed-season (modern empirical), and Rayleigh summer (east-derived). Groups are defined in Table 1; bold marks the preferred model for each group. Surface-uplift estimates are medians and 68% confidence intervals of the Monte Carlo distribution of elevation differences.

Group	Age (Ma)	*n*	Proxy	Winter (km)	Mixed-season (km)	Summer (km)
III	15.8–14.1	3	Glass δD	2.17 [1.44–3.03]	**2.62 [2.21–3.01]**	5.12 [4.03–6.28]
E	16.4–14.1	52	Carb. $\delta^{18}O$	1.88 [1.16–2.74]	**2.48 [2.03–2.89]**	4.73 [3.66–5.99]
D	17.8–16.5	34	Carb. $\delta^{18}O$	**2.25 [1.57–3.02]**	2.65 [2.28–3.01]	5.16 [4.18–6.20]
II	17.9	2	Glass δD	**1.54 [0.84–2.36]**	2.27 [1.82–2.72]	4.24 [3.22–5.41]
C	18.6–17.9	7	Carb. $\delta^{18}O$ (low)	**2.22 [1.54–2.98]**	2.63 [2.26–2.99]	5.11 [4.13–6.16]
B	18.8–18.3	9	Carb. $\delta^{18}O$ (high)	**0.52 [0.00–1.18]**	1.64 [1.25–2.07]	2.93 [2.11–3.92]
A	37–33	4	Carb. $\delta^{18}O$	**0.92 [0.20–1.87]**	1.90 [1.39–2.51]	3.51 [2.40–4.94]
Surface uplift (Group B → E), by model scenario:						
Winter → Mixed-season				**1,886 [1,446–2,255]** m		
Winter → Winter				1,288 [741–1,910] m		
Mixed-season → Mixed-season				818 [470–1,167] m		
Modern basin elevation: 2.36–2.90 km (mean 2.55 km)						

glass samples that pass our quality filters are interpreted to record environmental waters hydrating the glass 10^3–10^4 yr after eruption (Friedman et al., 1993). The $\delta^{18}O_{env,vg}$ values calculated from these samples are similar to or lower than $\delta^{18}O_{env,carb}$ from coeval carbonates (Figs. 4b–d & 5), whereas secondary spar samples show lower $\delta^{18}O_{carb}$ values, likely reflecting high-temperature crystallization following burial or hydration by near-surface fluids during exhumation at higher elevation (Fig. 4b; Quade et al., 2020). The close glass–micrite covariation, contrasted with consistently low spar $\delta^{18}O_{carb}$ values, argues against pervasive diagenetic resetting of micritic samples. Therefore, secondary alteration appears insufficient to explain the primary isotopic trends in our dataset.

5.2. Consideration of evaporative enrichment

Evaporative enrichment can elevate $\delta^{18}O_{carb}$ and δD_{vg} (Breecker et al., 2009; Nandy and Fan, 2025) and may raise $\delta^{13}C_{carb}$ via CO_2 outgassing (Horton et al., 2016). The lower Río de los Patos Formation contains abundant evaporite gypsum (Suriano et al., 2023) and yielded the highest $\delta^{18}O_{carb}$ value in our dataset (−6.31‰). Thus, this process likely influenced our Eocene samples, and corresponding paleoelevation estimates may be negatively biased.

Group B from the Chinches Formation yields similar $\delta^{18}O_{carb}$ values but lacks distinctive evaporite facies, and two lines of evidence argue against an evaporative mechanism controlling the 18.6–18.3 Ma

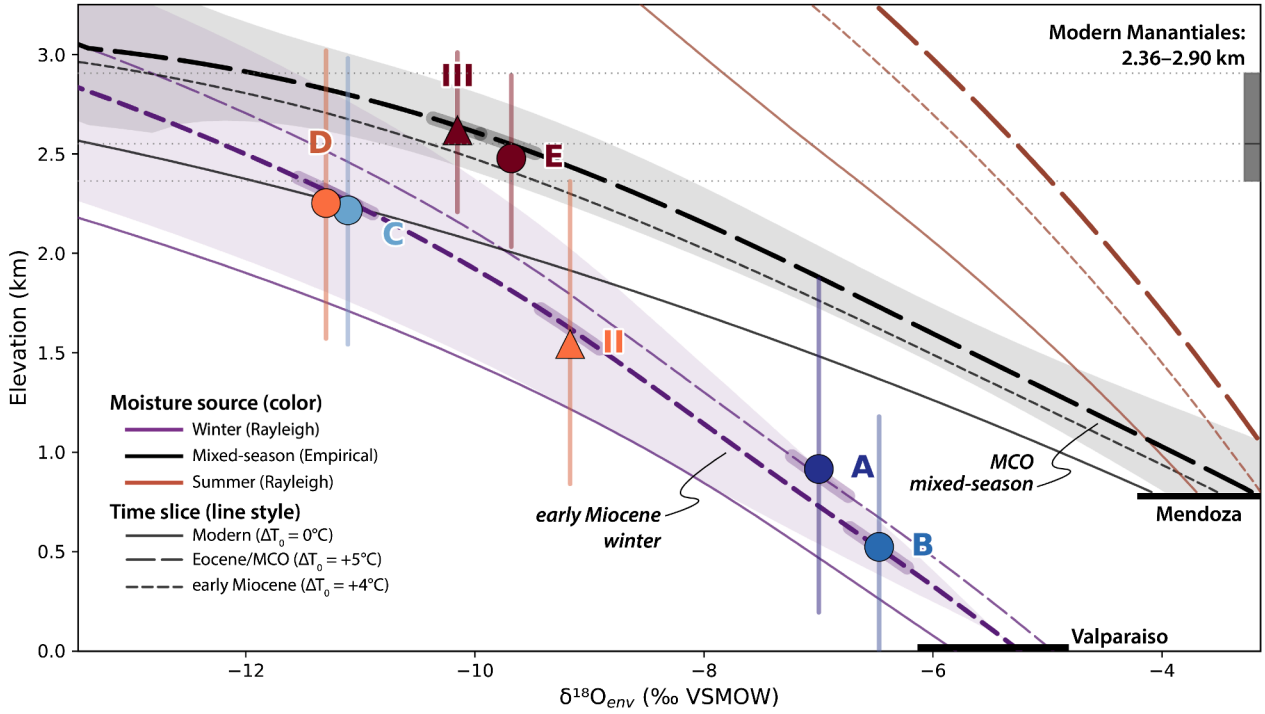

Fig. 6. Isotope–elevation relationships and preferred paleoelevation estimates by sample group. Curve color denotes the moisture source: winter Rayleigh (purple; Valparaíso source, sea level), mixed-season empirical (black), and summer Rayleigh (orange; Mendoza source, 0.80 km elevation). Solid curves are the modern relationships of Hoke et al. (2013); the remaining curves are the same models adjusted for past boundary conditions (Text S3): early Miocene (short-dashed; ΔT_0 = +4 °C) and Eocene/MCO (long-dashed; ΔT_0 = +5 °C). The Eocene and MCO boundary conditions share a central ΔT_0 of +5 °C and therefore plot as a single curve; the Eocene condition is drawn for the winter model only. Shaded envelopes show the $\pm 1\sigma$ model-uncertainty band for select curves (heavy lines). Each sample group is plotted at its median $\delta^{18}O_{env}$ and the elevation determined using its preferred model (highlighted): winter Rayleigh for Eocene–early Miocene groups (A, B, C, II, and D) and mixed-season empirical for MCO-interval groups (E, III). Vertical bars show 68% confidence intervals on elevation. Symbols match Fig. 5. The gray bar and tick at the right margin indicate the modern Manantiales basin elevation (2.36–2.90 km; mean 2.55 km).

decrease in $\delta^{18}O_{carb}$. First, the shift occurs within a continuously fluvial interval (Fig. 4), interpreted to record the onset of a transition to internal drainage (Ronemus et al., 2024). If this transition influenced the degree of evaporation, its predicted effect would be of the opposite sign. Second, this decrease is absent in bracketing samples from the Cacheuta basin, which occupied a foredeep position ~120 km to the SSE (Fig. 5; data from Hoke et al. 2014, recorrelated to the chronostratigraphy of Buelow et al. 2018); a regional climate-driven shift in evaporative intensity would be expected to imprint both basins. Lower post-shift $\delta^{18}O_{env}$ values are recorded concordantly by carbonates (Groups C & D) and glass (Group II), suggesting that waters plotted near the GMWL and were little evaporatively modified (Fig. 5). However, Group B predates our usable glass record and cannot be tested this way. We therefore cannot fully exclude an evaporative contribution, which would make our estimate of Group B to C surface uplift a maximum bound.

The rise in $\delta^{18}O_{carb}$ and $\delta^{13}C_{carb}$ values recorded after ca. 16.5 Ma coincides with establishment of internal basin drainage and resumption of sparse gypsum deposition (Fig. 4a–c; Ronemus et al., 2024). Calculated $\delta^{18}O_{env}$ for these samples exceeds that for coeval glass, consistent with declining deuterium excess and increasing evaporative enrichment (Fig. 5; Jimenez-Rodriguez et al., 2022; Li et al., 2022). Thus, evaporative enrichment may have contributed to higher $\delta^{18}O_{carb}$ and $\delta^{13}C_{carb}$ values in the Eocene and middle Miocene portions of the section, but it likely cannot account for the early Miocene step toward lower values.

5.3. The transition from an arid foredeep to an elevated wedge-top

To explain the early Miocene isotopic trends, we consider the effects of the proposed foredeep to wedge-top transition (Ronemus et al., 2024). Group B carbonates show high values of both $\delta^{18}O_{carb}$ (−7.9 ± 0.7 ‰) and $\delta^{13}C_{carb}$ (−2.0 ± 1.5 ‰) that overlap the range of bracketing values from the regional Cacheuta foredeep record (Fig. 5). We interpret these values to reflect weak orographic distillation at low altitude (Poage and Chamberlain, 2001) and sparse vegetation with low soil respiration rates under arid conditions (Cerling, 1984; Quade et al., 2007b), respectively. This interpretation is consistent with sedimentologic evidence that the basin occupied a low-elevation foredeep during its early evolution, when widespread arid conditions are recorded across the regional basin system (Fig. 8a–b; Jordan et al., 1996; Suriano et al., 2023; Starck et al., 2024; George et al., 2025). Limited moisture that did reach the basin over this interval was likely primarily delivered by the Pacific westerlies, which would not have been fully blocked by nascent Andean topography (see Text S3.6; Insel et al., 2010).

The subsequent shift to significantly lower values (Group C; $\delta^{18}O_{carb}$ = −12.5 ± 0.2 ‰; $\delta^{13}C_{carb}$ = −6.1 ± 1.8 ‰) by ca. 18.3 Ma diverges sharply from the Cacheuta record (Fig. 5). Because orographic distillation integrates over the moisture transport path, part of this shift could reflect uplift of an upwind topographic barrier (Fennell et al., 2023). However, the absence of a coeval shift in the Cacheuta record disfavors growth of western topography, which would imprint both basins, and instead points to surface uplift of the basin floor and/or immediately adjacent topography (Fig. 8c). The accompanying decrease in $\delta^{13}C_{carb}$ values is consistent with wetter conditions and enhanced soil productivity as orographic precipitation increased on the growing neighboring topography. This interpretation is corroborated by a basin-scale unconformity, shift to internal drainage, and change in sedimentary provenance, which Ronemus et al. (2024) interpreted to record transfer of the basin from a foredeep to a wedge-top position during uplift of the eastward-adjacent Cordillera del Tigre (ca. 19–15 Ma). Independent records provide additional evidence of renewed shortening, including inversion of the Abanico basin beginning ca. 18 Ma (Mpodozis et al., 2009; Perelló et al., 2012) and coeval exhumation of the Frontal Cordillera (Howlett et al.,

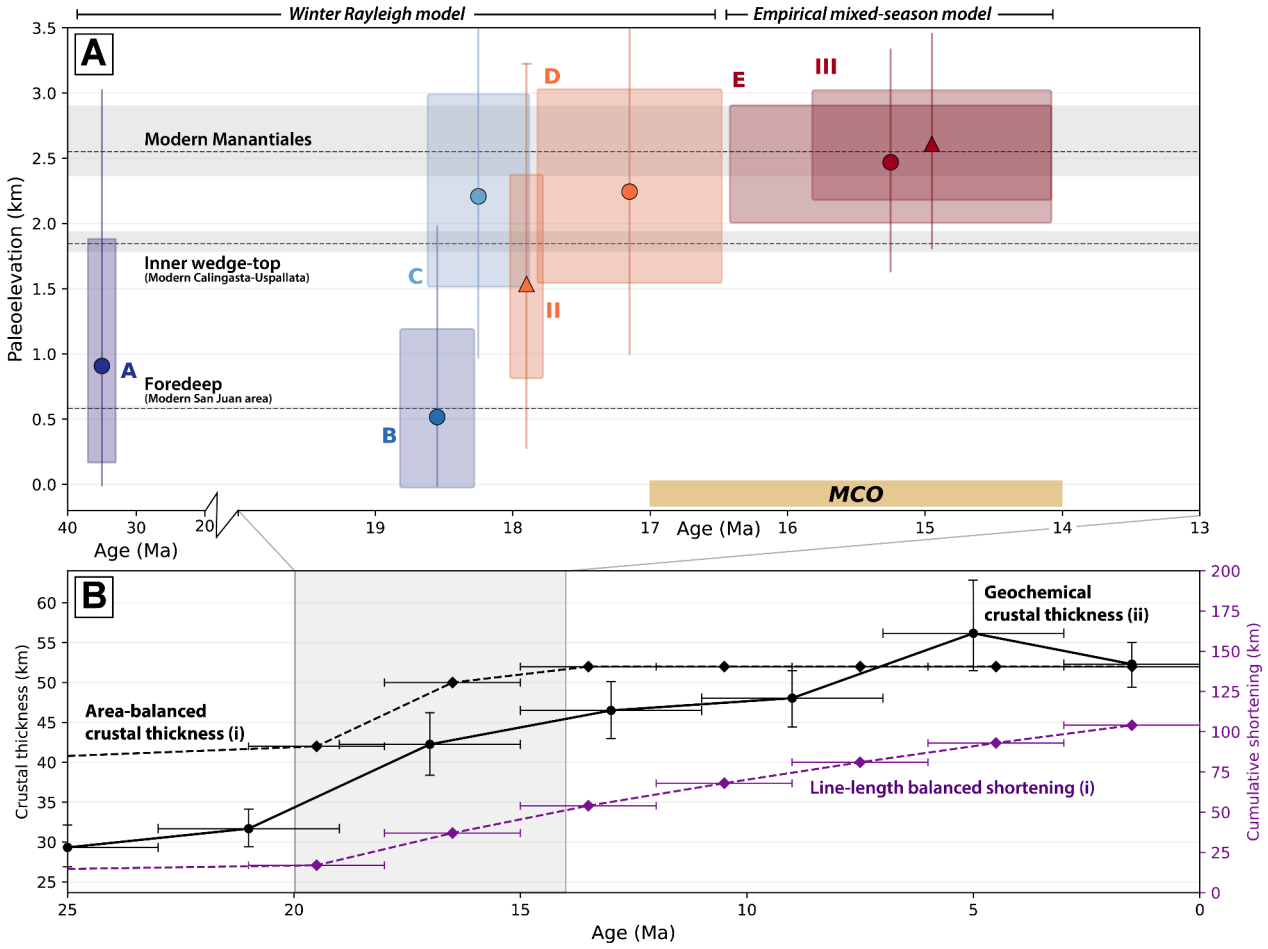

Fig. 7. (a) Preferred paleoelevation estimates through time. Each box spans the age range of its sample group on the *x*-axis and the 68% confidence interval on the *y*-axis; whiskers extend to the 95% confidence interval (truncated at the top of the panel for Groups C and D); symbols mark medians. Axis is broken at 20 Ma, showing Group A from the Río de los Patos Formation to the left and Chinches Formation groups to the right. Pre-MCO groups (A, B, C, II, D) are evaluated using the winter Rayleigh model and younger groups recording MCO conditions (E, III) using the mixed-season model. Groups are annotated and match symbols shown in Fig. 5. Horizontal black lines and envelopes indicate the mean and range of modern basins: Manantiales (~2.36–2.90 km; profile at 32°S in Fig. 1c); Calingasta-Uspallata (~1.78–1.96 km; profile at ~31.65°S); modern foreland east of the Precordillera (~0.57–0.60 km; profile at ~31.65°S). Full paleoelevation matrix is reported in Table 2. (b) Independent tectonic constraints at ~32°S. Left axis: Area-balanced crustal thickness from (i) Giambiagi et al. (2022) at 32.4°S (black diamonds, dashed line) and geochemical crustal thickness estimates from (ii) Muñoz-Gómez et al. (2025) at ~32.75–34.5°S (circles, solid line). Right axis: cumulative shortening from (i) Giambiagi et al. (2022) at 32.4°S (purple diamonds, dashed line).

2025). Surface uplift during the foredeep-to-wedge-top transfer has similarly been documented in the Eastern Cordillera (~25–26°S; Carrapa et al., 2014), suggesting a regional response to passage of the orogenic front.

5.4. Increasing $\delta^{18}O_{carb}$ and $\delta^{13}C_{carb}$ during MCO warming and continued shortening

After ca. 16.5 Ma, carbonate Group E records an increase in $\delta^{18}O_{carb}$ and $\delta^{13}C_{carb}$ whereas glass Group III records generally stable δD_{vg}. These trends complicate interpretation within a purely orographic context, because continued fold-thrust belt growth over this interval is suggested by thermochronology and growth strata evidence (Ronemus et al., 2024; Howlett et al., 2025) and would be expected to drive progressive orographic distillation and lower $\delta^{18}O_{carb}$ and δD_{vg}. This interval coincides with the MCO (ca. 17–14 Ma), and we evaluate the possible role of associated changes in temperature, evaporation intensity, or moisture source using our paired carbonate–glass stable-isotope record.

Through competing temperature effects on precipitation composition (Dansgaard, 1964) and calcite–water fractionation (Kim and O'Neil, 1997), imposed MCO warming of ~2–4 °C (conservatively large, see Text S5) would shift $\delta^{18}O_{carb}$ upward by a net ~+0.5–1.0‰, potentially accounting for part of the observed rise. However, the former effect would also raise glass δD values by ~+7–15‰, exceeding the carbonate response in comparable $\delta^{18}O_{env}$ terms because glass lacks the competing fractionation effect. Instead, δD_{vg} values of Group III remain low (−104.9 ± 4.8‰), suggesting that temperature change cannot be the sole driver of the observed stable-isotope trends.

Because δD_{vg} is less influenced by evaporation than $\delta^{18}O_{carb}$ (Jimenez-Rodriguez et al., 2022), enhanced evaporation as drainage in the Manantiales basin internalized could, in principle, account for the observed divergence of glass and carbonate records. However, the $\delta^{18}O_{carb}$ rise is recognized in the regional basin record (Fennell et al., 2023; George et al., 2025, and references therein) and spans diverse facies, rather than being confined to lacustrine or playa deposits (member 3; Fig. 4a–b). So, evaporation likely cannot account for the full signal.

The remaining candidate is a shift toward summer-derived moisture. Volcanic glass records amount-weighted mean annual precipitation (Cassel and Breecker, 2017), so an increase in summer moisture would raise δD_{vg} only in proportion to summer's share of the annual total. Pedogenic carbonate, by contrast, forms preferentially during warm-

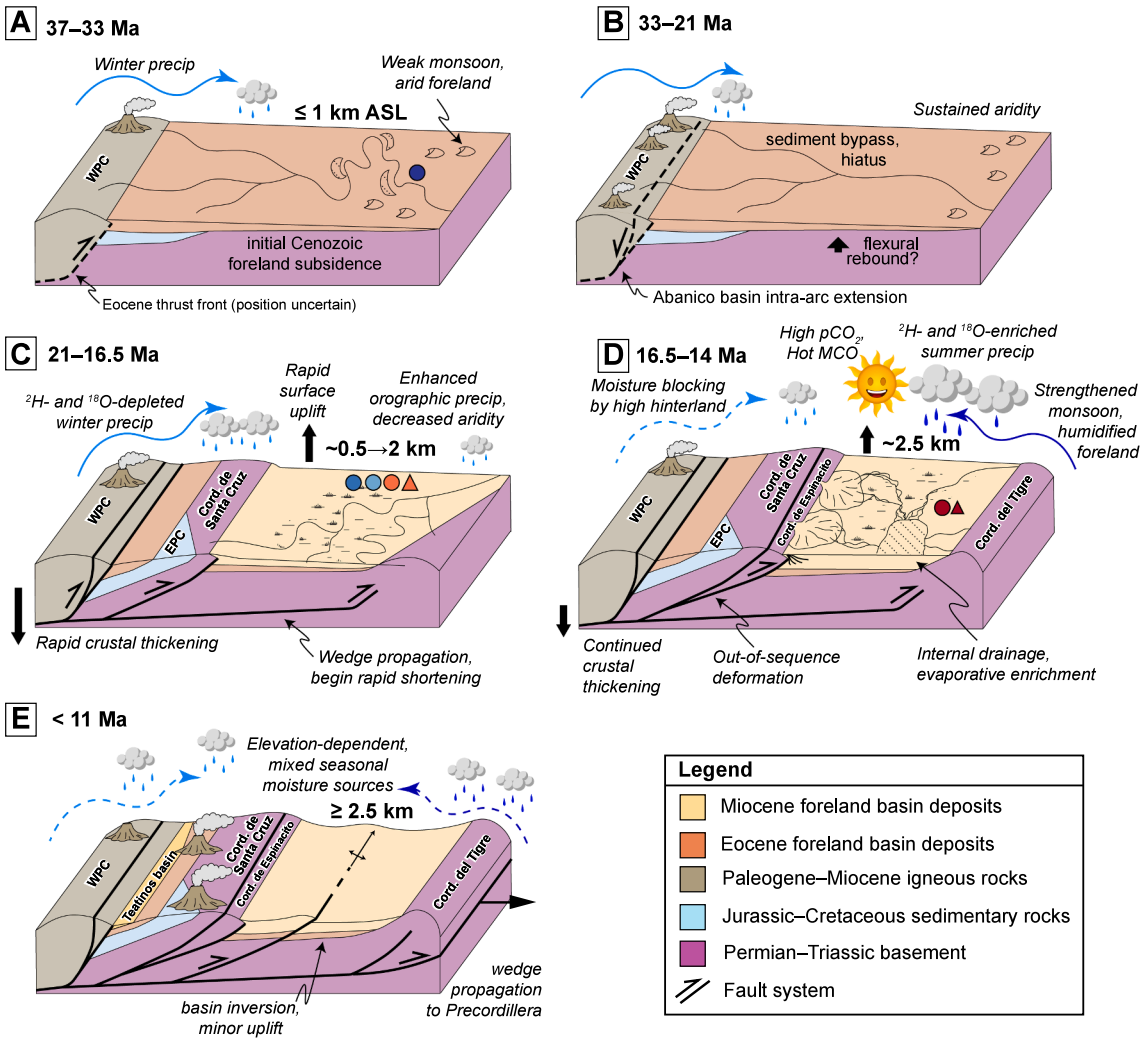

Fig. 8. Schematic block diagrams illustrating the tectonic, topographic, and climatic evolution of the Manantiales basin. (a) 37–33 Ma: The Cenozoic foreland basin initiates in a low-elevation (≤1 km) setting. Winter (Pacific-sourced) precipitation dominates across the low western barrier, yielding relatively high $\delta^{18}O_{carb}$ values; weak SASM limits summer moisture delivery, and sparse vegetation under arid conditions yields high $\delta^{13}C$ values. (b) 33–21 Ma: The Abanico intra-arc extensional basin develops in the Western Principal Cordillera, and sediment bypasses the basin during the depositional hiatus. Arid conditions persist regionally (George et al., 2025), but the interval is not sampled by our record. (c) 21–16.5 Ma: Deposition resumes as the Abanico basin inverts and shortening propagates rapidly eastward into the Frontal Cordillera. Crustal shortening and thickening drive surface uplift from ~0.5 to ~2 km as the basin is transferred to the wedge top, and growing topography adjacent to the basin enhances orographic distillation and reduces aridity, recorded by a step-wise isotopic shift. (d) 16.5–14 Ma: The basin reaches ~2.5 km elevation during the MCO. The high hinterland and out-of-sequence uplifts block low-$\delta^{18}O$ and -δD winter moisture while SASM intensification introduces higher-$\delta^{18}O$ and -δD summer precipitation. Along with development of internal drainage and evaporative enrichment, this partially masks continued uplift in $\delta^{18}O_{carb}$. (e) <11 Ma: Elevations of ~2.5 km are sustained as the basin inverts and the orogenic wedge propagates into the Precordillera. The moisture regime is presently dominated by summer (SASM) precipitation at low elevation and winter precipitation at higher elevation. The positions, geometries, and relationships of dashed faults are hypothetical and schematic, generally following: (a) Suriano et al. (2023), Ronemus et al. (2024), and Ronemus (2025, Appendix D); and (b) Jara and Charrier (2014). Miocene fault chronologies are synthesized from Jara and Charrier (2014), Mackaman-Lofland et al. (2020), Ronemus et al. (2024), Howlett et al. (2025), and Ronemus (2025, Appendix D). Teatinos basin after Peluffo et al. (2026). Colored circles and triangles correspond to sample groups in Figs. 5–7. WPC—Western Principal Cordillera; EPC—Eastern Principal Cordillera.

season drying windows following large precipitation events (Breecker et al., 2009; Huth et al., 2019), so the same moisture-source shift would be amplified in $\delta^{18}O_{carb}$. The coeval rise in $\delta^{13}C_{carb}$ is consistent with preferential carbonate formation under warm, well-ventilated summer soil conditions and with enhanced evaporative CO_2 outgassing (Cerling, 1984; Horton et al., 2016).

We propose that two developments drove a shift toward enhanced summer precipitation. First, MCO conditions strengthened the SASM (George et al., 2025), delivering higher-$\delta^{18}O$ and -δD Atlantic-derived moisture to the Manantiales basin (Fig. 8d). Second, accelerated shortening west of the basin after ca. 18 Ma raised the western orographic barrier (Mackaman-Lofland et al., 2020; Carrapa et al., 2022; Ronemus et al., 2024; Howlett et al., 2025), blocking lower-$\delta^{18}O$ and -δD Pacific-derived moisture and further amplifying the relative contribution of the SASM (Kleinert and Strecker, 2001; Ehlers and Poulsen, 2009; Insel et al., 2010). Because this western barrier persisted after the MCO waned, the shift toward summer-dominated precipitation was partly irreversible. Our isotope–elevation models simulating these temperature and moisture-source shifts suggest sustained to increasing basin paleoelevation over this interval, quantified below.

5.5. Paleoelevation synthesis and tectonic coupling

Using the winter Rayleigh model appropriate for the weak-SASM conditions inferred for the pre-MCO interval, the paleoelevations indicated for both Group A (Río de los Patos Formation) and Group B (lower Chinches Formation) are low and statistically indistinguishable from the modern foredeep (~0.6 km; Fig. 7a; Table 2). Therefore, we resolve no net change in basin-floor elevation across the intervening 33–21 Ma hiatus. All resolvable surface uplift postdates ca. 18.6 Ma, after which estimates (Groups II, C, & D) span the elevations of modern wedge-top basins and approach the modern basin elevation of 2.36–2.90 km. For samples spanning the MCO interval when significant summer moisture was likely introduced (Groups III, E), we favor the mixed-season model (Fig. 6; Hoke et al., 2013). Based on the carbonate record, the resulting total surface uplift from the lower to upper Chinches Formation is 1,886 m (68% CI: 1,446–2,255 m; Group B to E; Table 2). Despite not capturing the full uplift interval, the glass record yields a directionally consistent estimate of 1,060 m (338–1,697 m; Group II to III). Same-model comparisons for carbonate data yield 1,288 m (741–1,910 m; winter–winter) and 818 m (470–1,167 m; mixed-season–mixed-season). Surface uplift is resolved even at 95% confidence for the carbonate record in all three model pairings.

Regional records can be used as a further model-independent test (Fig. 5b). Pre-shift $\delta^{18}O_{env}$ values (Groups A–B) are similar to foredeep deposits of the Cacheuta and northern Uspallata basins, whereas post-shift values (Groups C–E) overlap with late Miocene(?) wedge-top deposits of the southern Uspallata basin (Fig. 5b; Hoke et al., 2014). Even during the MCO interval, $\delta^{18}O_{env}$ values in the Manantiales basin (Group E) remain ~1.3‰ lower than in the coeval Cacheuta foredeep, suggesting that the former occupied a higher position and/or was separated from the foredeep by intervening relief such as the Cordillera del Tigre (Fig. 5). These results further corroborate the foredeep-to-wedge-top transfer inferred from basin stratigraphy (Ronemus et al., 2024) and support our inference of Miocene surface uplift.

Overall, plausible scenarios yield substantial surface uplift coinciding with active crustal shortening, thickening, and fold-thrust belt exhumation documented independently within the region (Fig. 7; Carrapa et al., 2022; Mackaman-Lofland et al., 2020; Howlett et al., 2025). The most rapid phase (ca. 18.6–16.5 Ma) of surface uplift coincides with the onset of Abanico-basin inversion, rapid exhumation of the Frontal Cordillera, and the proposed transfer of the Manantiales basin to the wedge-top (Fig. 8b–c; Howlett et al., 2025; Jara and Charrier, 2014; Ronemus et al., 2024). Shortening subsequently shifted to out-of-sequence structures west of the basin, followed by propagation into the Precordillera to the east (Fig. 8d–e; Mackaman-Lofland et al., 2020; Ronemus et al., 2024; Howlett et al., 2025). This distributed shortening could have driven secondary regional surface uplift due to progressive eastward expansion of the crustal root, as proposed by Hoke et al. (2014). However, our preferred paleoelevation estimates already attain near-modern basin elevation by ca. 16.4–14 Ma (Groups E & III; Table 2), indicating that any subsequent uplift was modest.

5.6. Broader implications

Our findings affirm that unaccounted climate effects can produce spurious paleoaltimetry results. Applied across the MCO transition (Section 5.4), a single moisture-source scenario (winter model) yields a nominal elevation decrease from Group D to E (2.25 to 1.88 km; Table 2) despite continued crustal shortening and thickening. This is amplified under models not corrected for temperature change and may bias paleoelevation interpretations elsewhere in the Andes.

Indeed, our interpretation of coupled shortening, thickening, and surface uplift in the Manantiales basin stands in contrast to the Altiplano (~15–25°S), where large negative late Miocene shifts in $\delta^{18}O_{carb}$ and δD_{vg} have been attributed to rapid surface uplift following lithospheric foundering (e.g., Garzione et al., 2017; Sundell et al., 2019). One possible explanation for this apparent difference is that the southern Central Andes lacked Miocene crustal thicknesses sufficient to stabilize dense eclogite (Fig. 7b), required to drive the negative buoyancy that triggers foundering (Garzione et al., 2017). Alternatively, some portion of the late Miocene negative isotopic shifts on the Altiplano may reflect climate-driven overprinting analogous to, but in the opposite direction of, those documented here during the MCO (e.g., Ehlers and Poulsen, 2009).

The mechanisms considered here—including changes in aridity, moisture-source, evaporative enrichment, and temperature—are liable to compound elsewhere in the Andes and other orogens that evolved through climatic transition. For instance, the Malargüe basin (~35°S) records a sharp middle Miocene increase in δD_{vg} (Fennell et al., 2023) coinciding with eolianite disappearance (Starck et al., 2024; George et al., 2025) and crustal shortening and thickening to the west (Farías et al., 2008; Mescua et al., 2014; Muñoz-Gómez et al., 2025). Although topographic variation such as dynamic subsidence (Fennell et al., 2023) may have played a role, we speculate that this shift may be partially accounted for by the same orographic and climatic forcing described here, shifting that basin's precipitation budget toward ^{2}H-enriched SASM moisture. During the late Miocene, Carrapa et al. (2019) similarly argued that enhanced Hadley circulation drove regional $\delta^{18}O$ and $\delta^{13}C$ increases across the subtropical Andes. Our findings thus provide additional empirical support for modeling predictions that hydroclimate change during orogenic growth can mask or mimic surface uplift (Ehlers and Poulsen, 2009; Insel et al., 2010). Paired glass and carbonate proxies offer one strategy for disentangling these compounded signals.

6. Conclusions

Paired volcanic glass and pedogenic carbonate stable-isotope data from the Manantiales basin, evaluated against representative isotope–elevation models, constrain the timing and coupling of surface uplift to crustal shortening in the southern Central Andes at ~32°S. Our principal findings include:

1. High carbonate $\delta^{18}O$ and $\delta^{13}C$ values of pre-18.6 Ma samples reflect an arid, low-elevation setting under weak SASM circulation. Calculated paleoelevations assuming a winter-dominated precipitation regime are near those of the modern foredeep (Table 2; Fig. 7), consistent with the sedimentary record (Jordan et al., 1996; Suriano et al., 2023).
2. Carbonate records indicate ~1.9 km of syndepositional surface uplift at Manantiales, directionally corroborated by glass. Most uplift occurred between ca. 18.6 and 16.5 Ma during an interval of rapid crustal shortening and thickening and proposed transfer of the basin into the wedge-top depozone (Fig. 7b; Carrapa et al., 2022; Giambiagi et al., 2022; Ronemus et al., 2024). This result supports classical models of shortening-driven topographic growth in Cordilleran systems (Isacks, 1988; DeCelles et al., 2015) and contrasts with decoupled uplift suggested for the Altiplano (Garzione et al., 2017; Sundell et al., 2019).
3. After ca. 16.5 Ma, enhanced evaporation and increased relative summer moisture contribution, likely driven by warm MCO conditions (George et al., 2025) and orogenic uplift itself (Ehlers and Poulsen, 2009; Insel et al., 2010), raised carbonate $\delta^{18}O$ values and masked continued surface uplift in the isotopic record. Paired volcanic glass δD data help diagnose this overprinting because formation-season bias and evaporation have a greater influence on carbonate $\delta^{18}O$ than glass δD.

Together, these results indicate that surface uplift at ~32°S was coupled to upper crustal shortening, and provide empirical support for models showing how climate effects can compound tectonic signals in the stable-isotope record (Ehlers and Poulsen, 2009; Insel et al., 2010). In this context, paleoelevation histories at adjacent latitudes may warrant reassessment. Paired carbonate and glass stable-isotope data offer one

strategy for evaluating these effects in orogenic settings where topography and precipitation regime evolve in tandem.

CRediT authorship contribution statement

Chance B. Ronemus: Conceptualization, Methodology, Software, Formal analysis, Investigation, Data curation, Writing – original draft, Writing – review & editing, Visualization, Funding acquisition; **Caden J. Howlett:** Writing – review & editing, Investigation; **Peter G. DeCelles:** Investigation, Resources, Supervision, Funding acquisition, Writing – review & editing; **Barbara Carrapa:** Writing – review & editing, Supervision, Resources, Investigation, Funding acquisition; **Lucas M. Fennell:** Writing – review & editing, Resources, Investigation; **Kaustubh Thirumalai:** Investigation, Methodology, Resources, Supervision, Writing – review & editing; **Veleda A.P. Müller:** Investigation, Writing – review & editing; **Lucas Lothari:** Writing – review & editing, Resources, Investigation.

Ethics declaration

The authors declare that the study does not involve humans nor animal subjects.

Declaration of generative AI technologies in the manuscript preparation process

During the preparation of this work, the authors used Claude Code (Anthropic) within the Visual Studio Code IDE in order to help write, test, and comment analysis code deposited as Script S1. After using this tool, the authors reviewed and edited the content as needed and take full responsibility for the content of the published article.

Declaration of competing interest

The authors declare that they have no known competing financial interests or personal relationships that could have appeared to influence the work reported in this paper.

Acknowledgments

This study is part of the TransANdean Great Orogeny (TANGO) Project, funded by U.S. National Science Foundation (NSF) Grant EAR2020935. CBR conducted field components of this research as a Fulbright Research Scholar at IANIGLA CONICET, Mendoza, Argentina. He thanks the Fulbright Commission, Laura Giambiagi, José Mescua, Rodrigo Quiroga, Ahmad Arnous, Macarena Bertoa, Miranda Grover, and others who provided support during this exchange; Nicolás Peluffo is also thanked for field assistance. CBR acknowledges additional support from NSF EAR-PF #2518506, held at Idaho State University, and from the University of Arizona Coney Scholarship, the John and Nancy Sumner Scholarship, and Graduate and Professional Student Council Research and Project Grant funds. We thank Lin Li, Aniket Dhar, Xiaoyu Zhang, Cecilia A. Benavente, and David Dettman for assistance with analytical work. We thank Heather Alvarez and the University of Arizona Geosciences office staff for assistance with budgetary, travel, and sample shipment logistics. Finally, we thank Editor Andrew Zuza, Elizabeth Cassel, and an anonymous reviewer, whose feedback greatly improved this manuscript. We dedicate this manuscript to the memory of Dr. Jay Quade, who was involved with this project throughout but passed away before its completion; we express our sincere gratitude for Jay's innumerable contributions to isotope geochemistry throughout his career.

Data availability

Data and the analysis code (Script S1) supporting this study are available in the Zenodo repository at https://doi.org/10.5281/zenodo.23624845. The supporting text and datasets are also provided as supplementary material:

- Supporting Text: Sample descriptions, supplementary methods, isotope–elevation model rationale, and uncertainty propagation details
- Dataset S1: Volcanic glass isotope data (δD, H_2O)
- Dataset S2: Carbonate isotope data ($\delta^{18}O$, $\delta^{13}C$)

Supplementary material

Supplementary material associated with this article can be found in the online version at 10.1016/j.epsl.2026.120452.

References

Bookhagen, B., Strecker, M.R., 2008. Orographic barriers, high-resolution TRMM rainfall, and relief variations along the Eastern Andes. Geophys. Res. Lett. 35 (6), L06403. https://doi.org/10.1029/2007GL032011

Boschman, L.M., 2021. Andean mountain building since the late Cretaceous: a paleoelevation reconstruction. Earth-Science Rev. 220, 103640. https://doi.org/10.1016/j.earscirev.2021.103640

Breecker, D.O., Sharp, Z.D., McFadden, L.D., 2009. Seasonal bias in the formation and stable isotopic composition of pedogenic carbonate in modern soils from central New Mexico, USA. Geolog. Soc. Am. Bull. 121 (3-4), 630–640. https://doi.org/10.1130/B26413.1

Buelow, E.K., Suriano, J., Mahoney, J.B., Kimbrough, D.L., Mescua, J.F., Giambiagi, L.B., Hoke, G.D., 2018. Sedimentologic and stratigraphic evolution of the Cacheuta basin: constraints on the development of the Miocene retroarc foreland basin, South-Central Andes. Lithosphere 10 (3), 366–391. https://doi.org/10.1130/L709.1

Calvi, C., Carol, E., Fennell, L., Naipauer, M., 2024. Assessment of hydrological systems associated with groundwater discharges in arid high mountain environments of the Argentine Andes. Groundwater Sustain. Dev. 26, 101218. https://doi.org/10.1016/j.gsd.2024.101218

Canavan, R.R., Carrapa, B., Clementz, M.T., Quade, J., DeCelles, P.G., Schoenbohm, L.M., 2014. Early Cenozoic uplift of the Puna plateau, Central Andes, based on stable isotope paleoaltimetry of hydrated volcanic glass. Geology 42 (5), 447–450. https://doi.org/10.1130/G35239.1

Carrapa, B., Clementz, M., Feng, R., 2019. Ecological and hydroclimate responses to strengthening of the Hadley circulation in South America during the Late Miocene cooling. Proc. Natl. Acad. Sci. 116 (20), 9747–9752. https://doi.org/10.1073/pnas.1810721116

Carrapa, B., DeCelles, P.G., Ducea, M.N., Jepson, G., Osakwe, A., Balgord, E., Stevens Goddard, A.L., Giambiagi, L.A., 2022. Estimates of paleo-crustal thickness at Cerro Aconcagua (Southern Central Andes) from detrital proxy-records: implications for models of continental arc evolution. Earth Planet. Sci. Lett. 585, 117526. https://doi.org/10.1016/j.epsl.2022.117526

Carrapa, B., Huntington, K.W., Clementz, M., Quade, J., Bywater-Reyes, S., Schoenbohm, L.M., Canavan, R.R., 2014. Uplift of the Central Andes of NW Argentina associated with upper crustal shortening, revealed by multiproxy isotopic analyses. Tectonics 33 (6), 1039–1054. https://doi.org/10.1002/2013TC003461

Cassel, E.J., Breecker, D.O., 2017. Long-term stability of hydrogen isotope ratios in hydrated volcanic glass. Geochimica et Cosmochimica Acta 200, 67–86. https://doi.org/10.1016/j.gca.2016.12.001

Cerling, T.E., 1984. The stable isotopic composition of modern soil carbonate and its relationship to climate. Earth Planet. Sci. Lett. 71 (2), 229–240. https://doi.org/10.1016/0012-821X(84)90089-X

Charrier, R., Contreras, J.P., Díaz-Bórquez, C., Farías, M., Jara, P., Muñoz-Gómez, M., Quiñones, S., Rodríguez, M.P., Tapia, F., Villaseñor, T., 2024. The Cenozoic Abanico rift system: implications of increased southward extension in the southern central Andes, in Chile. J. South Am. Earth Sci. 148, 105159. https://doi.org/10.1016/j.jsames.2024.105159

Dansgaard, W., 1964. Stable isotopes in precipitation. Tellus A Dyn. Meteorol. Oceanogr. 16 (4), 436–468. https://doi.org/10.3402/tellusa.v16i4.8993

DeCelles, P.G., Giles, K.A., 1996. Foreland basin systems. Basin Res. 8 (2), 105–123. https://doi.org/10.1046/j.1365-2117.1996.01491.x

DeCelles, P.G., Zandt, G., Beck, S.L., Currie, C.A., Ducea, M.N., Kapp, P., Gehrels, G.E., Carrapa, B., Quade, J., Schoenbohm, L.M., 2015. Cyclical Orogenic Processes in the Cenozoic Central Andes. In: DeCelles, P.G., Ducea, M.N., Carrapa, B., Kapp, P.A. (Eds.), Geodynamics of a Cordilleran orogenic system: the Central Andes of Argentina and Northern Chile. Geological Society of America, Memoir 212, pp. 459–490. https://doi.org/10.1130/2015.1212(22)

Dettinger, M.P., Quade, J., 2015. Testing the analytical protocols and calibration of volcanic glass for the reconstruction of hydrogen isotopes in paleoprecipitation. In: DeCelles, P.G., Ducea, M.N., Carrapa, B., Kapp, P.A. (Eds.), Geodynamics of a Cordilleran Orogenic System: the Central Andes of Argentina and Northern Chile. Geological Society of America, Memoir 212, pp. 261–276. https://doi.org/10.1130/2015.1212(14)

Ehlers, T.A., Poulsen, C.J., 2009. Influence of Andean uplift on climate and paleoaltimetry estimates. Earth Planet. Sci. Lett. 281 (3), 238–248. https://doi.org/10.1016/j.epsl.2009.02.026

Farías, M., Charrier, R., Carretier, S., Martinod, J., Fock, A., Campbell, D., Cáceres, J., Comte, D., 2008. Late Miocene high and rapid surface uplift and its erosional response

in the Andes of central Chile (33°–35°S). Tectonics 27 (1), TC1005. https://doi.org/10.1029/2006TC002046

Fennell, L.M., Brandon, M.T., Hren, M.T., 2023. Cenozoic topographic evolution of the Southern Central Andes foreland as revealed by hydrogen stable isotopes in hydrated volcanic glass. Earth Planet. Sci. Lett. 604, 117991. https://doi.org/10.1016/j.epsl.2023.117991

Friedman, I., Gleason, J., Sheppard, R.A., Gude, A.J., 1993. Deuterium fractionation as water diffuses into silicic volcanic ash. In: Climate Change in Continental Isotopic Records. American Geophysical Union (AGU), pp. 321–323. https://doi.org/10.1029/GM078p0321

Garreaud, R.D., Vuille, M., Compagnucci, R., Marengo, J., 2009. Present-day South American climate. Palaeogeog. Palaeoclimatol. Palaeoecol. 281 (3), 180–195. https://doi.org/10.1016/j.palaeo.2007.10.032

Garzione, C.N., McQuarrie, N., Perez, N.D., Ehlers, T.A., Beck, S.L., Kar, N., Eichelberger, N., Chapman, A.D., Ward, K.M., Ducea, M.N., Lease, R.O., Poulsen, C.J., Wagner, L.S., Saylor, J.E., Zandt, G., Horton, B.K., 2017. Tectonic evolution of the Central Andean Plateau and implications for the growth of plateaus. Ann. Rev. Earth Planet. Sci. 45 (1), 529–559. https://doi.org/10.1146/annurev-earth-063016-020612

George, S.W.M., Carrapa, B., DeCelles, P.G., Jepson, G., Nadoya, H., Tabor, C., Howlett, C.J., Ronemus, C.B., Clementz, M.T., Schoenbohm, L., 2025. Increased moisture availability in the central Andes during the Miocene climatic optimum. Palaeogeogr. Palaeoclimatol. Palaeoecol. 663, 112732. https://doi.org/10.1016/j.palaeo.2025.112732

Giambiagi, L.B., Tassara, A., Echaurren, A., Julve, J., Quiroga, R., Barrionuevo, M., Liu, S., Echeverría, I., Mardónez, D., Suriano, J., Mescua, J., Lossada, A.C., Spagnotto, S., Bertoa, M., Lothari, L., 2022. Crustal anatomy and evolution of a subduction-related orogenic system: insights from the Southern Central Andes (22-35°S). Earth-Science Rev. 232, 104138. https://doi.org/10.1016/j.earscirev.2022.104138

Goldner, A., Herold, N., Huber, M., 2014. The challenge of simulating the warmth of the mid-Miocene climatic optimum in CESM1. Clim. Past 10 (2), 523–536. https://doi.org/10.5194/cp-10-523-2014

Hoke, G.D., Aranibar, J.N., Viale, M., Araneo, D.C., Llano, C., 2013. Seasonal moisture sources and the isotopic composition of precipitation, rivers, and carbonates across the Andes at 32.5–35.5°S. Geochem. Geophys. Geosyst. 14 (4), 962–978. https://doi.org/10.1002/ggge.20045

Hoke, G.D., Giambiagi, L.B., Garzione, C.N., Mahoney, J.B., Strecker, M.R., 2014. Neogene paleoelevation of intermontane basins in a narrow, compressional mountain range, southern Central Andes of Argentina. Earth Planet. Sci. Lett. 406, 153–164. https://doi.org/10.1016/j.epsl.2014.08.032

Horton, T.W., Defliese, W.F., Tripati, A.K., Oze, C., 2016. Evaporation induced ^{18}O and ^{13}C enrichment in lake systems: a global perspective on hydrologic balance effects. Quatern. Sci. Rev. 131, 365–379. https://doi.org/10.1016/j.quascirev.2015.06.030

Howlett, C.J., Ronemus, C.B., Carrapa, B., DeCelles, P.G., 2025. Miocene construction of the High Andes recorded by exhumation of the Frontal Cordillera, La Ramada Massif of Western Argentina (32°S). Tectonics 44 (1), e2024TC008433. https://doi.org/10.1029/2024TC008433

Huth, T.E., Cerling, T.E., Marchetti, D.W., Bowling, D.R., Ellwein, A.L., Passey, B.H., 2019. Seasonal bias in soil carbonate formation and its implications for interpreting high-resolution paleoarchives: evidence from southern Utah. J. Geophys. Res. Biogeosci. 124 (3), 616–632. https://doi.org/10.1029/2018JG004496

Insel, N., Poulsen, C.J., Ehlers, T.A., 2010. Influence of the Andes mountains on South American moisture transport, convection, and precipitation. Clim. Dyn. 35 (7), 1477–1492. https://doi.org/10.1007/s00382-009-0637-1

Insel, N., Poulsen, C.J., Sturm, C., Ehlers, T.A., 2013. Climate controls on Andean precipitation $\delta^{18}O$ interannual variability. J. Geophys. Res. Atmosph. 118 (17), 9721–9742. https://doi.org/10.1002/jgrd.50619

Isacks, B.L., 1988. Uplift of the central Andean plateau and bending of the Bolivian Orocline. J. Geophys. Res. 93 (B4), 3211–3231. https://doi.org/10.1029/JB093iB04p03211

Jara, P., Charrier, R., 2014. Nuevos antecedentes estratigráficos y geocronológicos para el Meso-Cenozoico de la Cordillera Principal de Chile entre 32° y 32°30'S: implicancias estructurales y paleogeográficas. Andean Geol. 41 (1), 174–209. https://doi.org/10.5027/andgeoV41n1-a07

Jimenez-Rodriguez, S., Quade, J., Dettinger, M., Huntington, K.W., Kelson, J.R., 2022. Comparing isotopic estimates of paleoelevation from carbonates and volcanic glass from the Miocene-age Chucal Formation in northern Chile. Chem. Geol. 596, 120798. https://doi.org/10.1016/j.chemgeo.2022.120798

Jordan, T.E., Tamm, V., Figueroa, G., Flemings, P.B., Richards, D., Tabbutt, K., Cheatham, T., 1996. Development of the Miocene Manantiales foreland basin, Principal Cordillera, San Juan, Argentina. Andean Geol. 23 (1), 43–79.

Kim, S.-T., O'Neil, J.R., 1997. Equilibrium and nonequilibrium oxygen isotope effects in synthetic carbonates. Geochimica et Cosmochimica Acta 61 (16), 3461–3475. https://doi.org/10.1016/S0016-7037(97)00169-5

Kleinert, K., Strecker, M.R., 2001. Climate change in response to orographic barrier uplift: paleosol and stable isotope evidence from the late Neogene Santa María basin, Northwestern Argentina. GSA Bull. 113 (6), 728–742. https://doi.org/10.1130/0016-7606(2001)113<0728:CCIRTO>2.0.CO;2

Li, L., Lu, H., Garzione, C., Fan, M., 2022. Cenozoic paleoelevation history of the Lunpola Basin in Central Tibet: new evidence from volcanic glass hydrogen isotopes and a critical review. Earth-Science Rev. 231, 104068. https://doi.org/10.1016/j.earscirev.2022.104068

Mackaman-Lofland, C., Horton, B.K., Fuentes, F., Constenius, K.N., Ketcham, R.A., Capaldi, T.N., Stockli, D.F., Ammirati, J.-B., Alvarado, P., Orozco, P., 2020. Andean mountain building and foreland basin evolution during thin- and thick-skinned Neogene deformation (32–33°S). Tectonics 39 (3), e2019TC005838. https://doi.org/10.1029/2019TC005838

Mescua, J.F., Giambiagi, L.B., Tassara, A., Gimenez, M., Ramos, V.A., 2014. Influence of pre-Andean history over Cenozoic foreland deformation: structural styles in the Malargüe fold-and-thrust belt at 35°S, Andes of Argentina. Geosphere 10 (3), 585–609. https://doi.org/10.1130/GES00939.1

Miller, K.G., Browning, J.V., Schmelz, W.J., Kopp, R.E., Mountain, G.S., Wright, J.D., 2020. Cenozoic sea-level and cryospheric evolution from deep-sea geochemical and continental margin records. Sci. Adv. 6 (20), eaaz1346. https://doi.org/10.1126/sciadv.aaz1346

Mpodozis, C., Brockway, H., Marquardt, C., Perelló, J., 2009. Geocronología U-Pb y tectónica de la región Los Pelambres-Cerro Mercedario: Implicancias para la evolución cenozoica de los Andes del centro de Chile y Argentina. In: Congreso Geológico Chileno. No. 12. Santiago.

Muñoz-Gómez, M., Fanning, C.M., Tapia, F., Payacán, I., Fuentes, F., Farías, M., Charrier, R., Polvé, M., Quiñones, S., Deckart, K., Fock, A., 2025. Resolving crustal and subcrustal dynamic sources in continental arc magmas: the Cenozoic Andean arc of Central Chile. Geochem. Geophys. Geosyst. 26 (9), e2024GC012154. https://doi.org/10.1029/2024GC012154

Nandy, R., Fan, M., 2025. A new procedure for volcanic glass hydrogen isotope studies of tuffaceous sediments and its application in the North American Cordillera. GSA Bull. 137 (5-6), 2647–2660. https://doi.org/10.1130/B37783.1

Peluffo, N.A., Fennell, L.M., Thomas, S.E., Martos, F.E., Valencia, V., Folguera, A., Naipauer, M., 2026. Polyphasic deformation during the evolution of the southern Central Andes: insights from the La Ramada fold-thrust belt (32°-32°30′S). Tectonophysics 923, 231070. https://doi.org/10.1016/j.tecto.2026.231070

Perelló, J., Sillitoe, R.H., Mpodozis, C., Brockway, H., Posso, H., 2012. Geologic Setting and Evolution of the Porphyry Copper-Molybdenum and Copper-Gold Deposits at Los Pelambres, Central Chile. Society of Economic Geologists, Special Publication 16, pp. 79–104. https://doi.org/10.5382/SP.16.04

Peters, N.A., Huntington, K.W., Hoke, G.D., 2013. Hot or not? Impact of seasonally variable soil carbonate formation on paleotemperature and O-isotope records from clumped isotope thermometry. Earth Planet. Sci. Lett. 361, 208–218. https://doi.org/10.1016/j.epsl.2012.10.024

Pinto, L., Alarcón, P., Morton, A., Naipauer, M., 2018. Geochemistry of heavy minerals and U–Pb detrital zircon geochronology in the Manantiales basin: implications for Frontal Cordillera uplift and foreland basin connectivity in the Andes of central Argentina. Palaeogeogr. Palaeoclimatol. Palaeoecol. 492, 104–125. https://doi.org/10.1016/j.palaeo.2017.12.017

Poage, M.A., Chamberlain, C.P., 2001. Empirical relationships between elevation and the stable isotope composition of precipitation and surface waters: considerations for studies of paleoelevation change. Am. J. Sci. 301 (1), 1–15. https://doi.org/10.2475/ajs.301.1.1

Quade, J., Dettinger, M.P., Carrapa, B., DeCelles, P., Murray, K.E., Huntington, K.W., Cartwright, A., Canavan, R.R., Gehrels, G., Clementz, M., 2015. The Growth of the Central Andes, 22°S–26°S. In: DeCelles, P.G., Ducea, M.N., Carrapa, B., Kapp, P.A. (Eds.), Geodynamics of a Cordilleran orogenic system: the Central Andes of Argentina and Northern Chile. Geological Society of America, Memoir 212, pp. 277–308. https://doi.org/10.1130/2015.1212(15)

Quade, J., Garzione, C., Eiler, J., 2007a. Paleoelevation reconstruction using pedogenic carbonates. Rev. Mineral. Geochem. 66 (1), 53–87. https://doi.org/10.2138/rmg.2007.66.3

Quade, J., Leary, R., Dettinger, M.P., Orme, D., Krupa, A., DeCelles, P.G., Kano, A., Kato, H., Waldrip, R., Huang, W., Kapp, P., 2020. Resetting Southern Tibet: the serious challenge of obtaining primary records of paleoaltimetry. Global Planet. Change 191, 103194. https://doi.org/10.1016/j.gloplacha.2020.103194

Quade, J., Rech, J.A., Latorre, C., Betancourt, J.L., Gleeson, E., Kalin, M. T.K., 2007b. Soils at the hyperarid margin: the isotopic composition of soil carbonate from the Atacama desert, Northern Chile. Geochimica et Cosmochimica Acta 71 (15), 3772–3795. https://doi.org/10.1016/j.gca.2007.02.016

Ramos, V.A., 2009. Anatomy and global context of the Andes: main geologic features and the Andean orogenic cycle. In: Kay, S.M., Ramos, V.A., Dickinson, W.R. (Eds.), Backbone of the Americas: Shallow Subduction, Plateau Uplift, and Ridge and Terrane Collision. Geological Society of America, Memoir 204, pp. 31–65. https://doi.org/10.1130/2009.1204(02)

Rocher, S., Alasino, P.H., Dahlquist, J.A., Basei, M. A.S., 2024. Permian-Triassic volcanic and plutonic records of the Argentine Frontal Cordillera: a review with new U–Pb and Hf-isotope zircon data. J. South Am. Earth Sci. 149, 105181. https://doi.org/10.1016/j.jsames.2024.105181

Rohrmann, A., Strecker, M.R., Bookhagen, B., Mulch, A., Sachse, D., Pingel, H., Alonso, R.N., Schildgen, T.F., Montero, C., 2014. Can stable isotopes ride out the storms? The role of convection for water isotopes in models, records, and paleoaltimetry studies in the central Andes. Earth Planet. Sci. Lett. 407, 187–195. https://doi.org/10.1016/j.epsl.2014.09.021

Ronemus, C.B., 2025. Cretaceous to Cenozoic Evolution of the Southern Central Andes and Basins Therein. Ph.D. thesis. University of Arizona. Tucson, AZ.

Ronemus, C.B., Howlett, C.J., DeCelles, P.G., Carrapa, B., George, S. W.M., 2024. The Manantiales basin, southern Central Andes (~32°S), preserves a record of late Eocene–Miocene episodic growth of an east-vergent orogenic wedge. Tectonics 43 (3), e2023TC008100. https://doi.org/10.1029/2023TC008100

Rowley, D.B., 2007. Stable isotope-based paleoaltimetry: theory and validation. Rev. Mineral. Geochem. 66 (1), 23–52. https://doi.org/10.2138/rmg.2007.66.2

Rowley, D.B., Pierrehumbert, R.T., Currie, B.S., 2001. A new approach to stable isotope-based paleoaltimetry: implications for paleoaltimetry and paleohypsometry of the High Himalaya since the late Miocene. Earth Planet. Sci. Lett. 188 (1), 253–268. https://doi.org/10.1016/S0012-821X(01)00324-7

Ruskin, B.G., Jordan, T.E., 2007. Climate change across continental sequence boundaries: Paleopedology and Lithofacies of Iglesia basin, Northwestern Argentina. J. Sediment. Res. 77 (9), 661–679. https://doi.org/10.2110/jsr.2007.069

Seligman, A.N., Bindeman, I.N., Watkins, J.M., Ross, A.M., 2016. Water in volcanic glass: from volcanic degassing to secondary hydration. Geochimica et Cosmochimica Acta 191, 216–238. https://doi.org/10.1016/j.gca.2016.07.010

Starck, D., Capaldi, T.N., Fuentes, F., Horton, B.K., 2024. Tectonic and climatic significance of Oligocene-Miocene eolian sandstones in the Andean foreland basin of Argentina. J. South Am. Earth Sci. 134, 104758. https://doi.org/10.1016/j.jsames.2023.104758

Sundell, K.E., Saylor, J.E., Lapen, T.J., Horton, B.K., 2019. Implications of variable late Cenozoic surface uplift across the Peruvian central Andes. Scient. Rep. 9 (1), 4877. https://doi.org/10.1038/s41598-019-41257-3

Super, J.R., Thomas, E., Pagani, M., Huber, M., O'Brien, C., Hull, P.M., 2018. North Atlantic temperature and pCO_2 coupling in the early-middle Miocene. Geology 46 (6), 519–522. https://doi.org/10.1130/G40228.1

Suriano, J., Lossada, A.C., Mahoney, J.B., Tedesco, A.M., Limarino, C.O., Giambiagi, L.B., Mazzitelli, M.A., Mescua, J.F., Lothari, L., Quiroga, R., 2023. The southern extension of the Eocene Andean orogeny: new sedimentary record of the foreland basin in the southern Central Andes at 32° S. Basin Res. 35 (6), 2381–2400. https://doi.org/10.1111/bre.12803

Vuille, M., Burns, S.J., Taylor, B.L., Cruz, F.W., Bird, B.W., Abbott, M.B., Kanner, L.C., Cheng, H., Novello, V.F., 2012. A review of the South American monsoon history as recorded in stable isotopic proxies over the past two millennia. Clim. Past 8 (4), 1309–1321. https://doi.org/10.5194/cp-8-1309-2012

White, E.J., Cassel, E.J., Breecker, D.O., 2024. Abrupt geographic shift in hydrogen isotope ratios of meteoric water across the Western Andes, Peru. Geophys. Res. Lett. 51 (5), e2023GL107098. https://doi.org/10.1029/2023GL107098